PARAMETERS FOR LOAD TRANSFER ANALYSIS OF ENERGY PILES IN UNIFORM NON-PLASTIC SOILS

By Diming Chen, M.S.[1] and John S. McCartney, Ph.D., P.E., M.ASCE[2]

Abstract: This study focuses on the use of a thermo-mechanical soil-structure interaction (load transfer) analysis to assess the axial strains, stresses, and displacements during thermo-mechanical loading of energy piles in various soil deposits and having different end restraint boundary conditions. After providing details of the model and its novel features, this paper presents a parametric evaluation performed to understand the roles of the soil shear strength parameters, toe stiffness, head stiffness, side shear stress-displacement curve, and radial expansion, as well as the magnitude of temperature change. This evaluation showed that the end restraint boundary conditions play the most important role in controlling the magnitude and location of the maximum thermal axial stress. The soil type also causes changes in the nonlinearity of the axial stress distribution throughout the energy pile. The radial expansion did not affect the thermo-mechanical soil-structure interaction for the conditions investigated in this study. The thermo-mechanical load-transfer analysis was then calibrated to identify the parameters that match the observed soil-structure interaction responses from four case studies of energy piles in non-plastic soil or rock layers during monotonic heating, including one field study and three centrifuge studies. The ranges of calibrated parameters provide insight into the behavior of energy piles in non-plastic soils, and can be used for preliminary design guidance.

[1] Graduate Student, Dept. of Structural Eng., Univ. of California San Diego, 9500 Gilman Dr., La Jolla, CA 92093-0085; dic022@eng.ucsd.edu
[2] Associate Professor, Dept. of Structural Eng., Univ. of California San Diego, 9500 Gilman Dr., La Jolla, CA 92093-0085; mccartney@ucsd.edu

INTRODUCTION

Energy piles are a dual-purpose structural element built underground to exchange heat between a building and the subsurface while also transferring loads from the structure to the ground. Different from classical deep foundations, energy piles incorporate closed-loop, flexible, high density polyethylene (HDPE) tubing within the reinforcing cage, through which a heat exchange fluid (i.e., typically water mixed with propylene glycol) is circulated to transfer heat to or from the subsurface. The temperature of the fluid is controlled using a heat pump within the building. The relatively steady temperature of subsurface soil and rock below 3 to 5 m is approximately equal to the mean annual air temperature (Burger et al. 1985), which makes it a stable heat source for efficient heat exchange needed to cover the base heating and cooling thermal loads for a built structure (Brandl 2006).

Geotechnical design of energy piles requires consideration of the impact of temperature on the induced stresses and strains in the pile, which may affect building performance. Specifically, heating and cooling of the pile during heat exchange will lead to expansion and contraction of the pile and soil. This may lead to deformations and changes in the stress state (Brandl 2006; Laloui and Nuth 2006; Bourne-Webb et al. 2009). Therefore, it is important for designers to understand the thermo-mechanical behavior of energy piles in various soil or rock deposits expected for different temperature changes.

There are many means to simulate the thermo-mechanical behavior of energy piles. For example, the mechanisms of thermo-mechanical soil-structure interaction have been documented in several full-scale case histories in the field (Laloui et al. 2003; Brandl 2006; Laloui et al. 2006; Bourne-Webb et al. 2009; Amatya et al. 2012; McCartney and Murphy 2012; Akrouch et al. 2014; Sutman et al. 2014; Murphy et al. 2015; Murphy and McCartney 2015; Olgun et al. 2014a; Wang et al. 2014). Although these studies provide insight into the mechanisms governing energy pile behavior, this behavior must be synthesized into the form of a model to provide quantitative predictions of energy pile behavior in different settings. Thermoelastic finite-element (FE) analyses have also been used to predict the changes in axial displacement, strain, and stress in energy piles during heating and cooling (Laloui et al. 2006; Ouyang et al. 2011; Wang et al. 2012, 2015; Rotta Loria et al. 2015a, 2015b). However, FE analyses are complicated to perform for energy pile design due to the large number of parameters potentially needed that may require advanced testing to obtain, especially when nonlinear soil behavior is considered. Alternatively, a comparably simpler method referred to as the thermo-mechanical load transfer analyses can be used to predict the behavior of energy piles under temperature changes (Knellwolf et al. 2011; Plaseied 2012; Suryatriyastuti et al. 2013). This method combines a known or assumed shape of the mobilized side shear resistance and end bearing resistance curves together with knowledge of the ultimate side shear and end bearing capacities to estimate the distribution in mobilized axial stress, strain and displacement with depth. Although this approach is simpler and requires fewer parameters to consider nonlinear soil-pile interaction, there is limited information on the range of parameters that describe the shapes of the mobilized side shear resistance and end bearing resistance curves of energy piles needed to perform thermo-mechanical load transfer analyses.

The main objective of this study is to understand the effects of model parameters on the output of the load transfer analyses to understand the relative importance of the different variables. Another equally important objective is to understand typical ranges of model parameters calibrated using experimental data associated with the thermo-mechanical behavior of energy piles having different end-restraint boundary conditions in non-plastic soils where soil thermal volume changes are not expected. To reach these objectives, the thermo-mechanical load transfer analysis described by Plaseied (2012) and McCartney (2015) was updated to better identify the null point location (the location of zero thermal displacement in an energy pile undergoing a uniform temperature change) and to incorporate different models for the side shear resistance of soils under drained and undrained conditions. Next, a parametric evaluation was performed to understand the effects of different parameters on the stress-strain response. Then, the model was fitted to the experimental results from four different studies to calibrate the different model parameters. Finally, ranges and trends in the calibrated model parameters were synthesized to provide design guidance.

BACKGROUND

Subsurface geothermal resources represent a great potential of directly usable energy, especially in connection with deep foundations and heat pumps. It is already common to utilize the geothermal energy in providing thermal needs of buildings. To utilize subsurface geothermal energy, a heat exchanger is commonly incorporated into drilled shaft foundations for circulating heat exchange fluid between the subsurface ground and a structure. However, it also presents new challenges for the broader geotechnical engineering profession in terms of technical issues associated with soil-structure interaction (Laloui et al. 2006; Bourne-Webb et al. 2009; Amatya et al. 2012; Murphy et al. 2015).

Observations from several case histories involving full-scale energy piles indicate that heating and cooling will lead to movements associated with thermal expansion and contraction of the pile element and surrounding soil (Laloui et al. 2003; Brandl 2006; Laloui et al. 2006; Bourne-Webb et al. 2009; Amatya et al. 2012; McCartney and Murphy 2012; Akrouch et al. 2014; Sutman et al. 2014; Olgun et al. 2014a; Wang et al. 2014; Murphy et al. 2015; Murphy and McCartney 2015). These thermally-induced movements may lead to the generation of axial stresses due to the restraint of the pile provided by soil-structure interaction and end-restraint boundary conditions (i.e., the stiffness of the overlying structure and the underlying bearing layer). Lateral movements of energy piles during heating and cooling has been proposed as a mechanism of changing soil structure interaction (McCartney and Rosenberg 2011; Mimouni and Laloui 2014), although cavity expansion analyses indicate that the amount of lateral expansion may not be sufficient to change the lateral stress state in all soils profiles (Olgun et al. 2014b). The end-restraint boundary conditions play an important role in design guidelines being proposed for energy piles (Suryatriyastuti et al. 2013; Mimouni and Laloui 2014). As it is often difficult to vary the end-restraint boundary conditions in full-scale energy pile systems to investigate their impact on soil-structure interaction mechanisms, an alternate modeling approach involves the use of centrifuge-scale energy (McCartney and Rosenberg 2011; Stewart and McCartney 2014; Goode et al. 2014; Goode and McCartney 2014; Goode and McCartney 2015; Ng et al. 2014, 2015). Although centrifuge tests represent an idealized situation compared to field tests and may not properly consider the role of construction effects, they have been shown to be useful for calibration or validation of numerical simulations using thermo-elasto-plastic finite element models or load transfer analyses.

One of the first studies to modify the conventional load transfer analysis for mechanical loading to consider thermo-mechanical load transfer analysis was performed by Knellwolf et al. (2011), where the energy pile was assumed to consist of elastic pile elements connected to the soil by elastic perfectly-plastic springs. Plaseied (2012) developed a load transfer analysis by considering nonlinear springs, where the mobilized side shear and end bearing resistance springs were represented by hyperbolic curves. Plaseied (2012) also considered the role of radial expansion of the pile elements, but did not perform a through parametric evaluation of this parameter. The algorithm in the model of Plaseied (2012) also fails to capture the exact location of the null point, and requires the user to choose the null-point, which leads to potentially inaccurate results.

Thermo-mechanical load transfer analyses have been validated on the basis of in-situ measurements of the loads and deformations experienced by heat exchanger test piles (Knellwolf et al. 2011; Plaseied 2012), but the choice of parameters for this method needs to be further studied in order to put this method to practical use. Energy pile design guidelines to account for thermal soil-structure interaction effects are available in different countries (Burlon et al. 2013; Mimouni and Laloui 2014; Bourne-Webb et al. 2014), but there is still a need for consistent soil-structure guidance to ensure implementation in practice worldwide.

LOAD TRANSFER ANALYSIS DESCRIPTION

Theory

An axial load transfer analysis is developed in this study to predict the behavior of energy piles subject to combined mechanical and thermal loading. The thermo-mechanical load transfer analysis is based on the following assumptions:

1. The properties of the pile such as the Young's modulus (E) and coefficient of thermal expansion (α_T) remain constant along the pile.
2. Downward and upward movements are taken as positive and negative respectively. Compressional stresses and forces are also taken to be positive.
3. The pile expands and contracts about a point referred to as the null point when it is heated or cooled (Bourne-Webb et al. 2009). The location of the null point depends on the upper and lower axial boundary conditions and side shear distribution, and will be defined later. Expansion strains are assumed to be negative.

4. Depending on the particular details of the soil profile, the ultimate side shear resistance can be assumed to be constant with depth in a soil layer (i.e., the α method) (Tomlinson 1957) or it can be assumed to increase linearly with depth in a soil profile (i.e., the β method) (Rollins et al. 1997). Both approaches are used in the parametric analysis.

The following notations are used in the thermo-mechanical load transfer analysis: Q is used to represent axial forces within the pile or on the pile boundaries; the letter ρ stands for the axial displacement of the pile, K_f, K_s and K_{base} are the stiffness values of the reinforced concrete pile spring, the side shear spring, and the base spring, respectively; the indices "*b*", "*t*" and "*s*" represent the bottom, top and side of an element; the indices *M*, *T*, *MT* stand for mechanical, thermal loading and thermo-mechanical loading, respectively; the superscript "*i*" represents the element number within the pile; and the variable "L^i" represents the length of each element along the pile.

Considering a pile under mechanical loading, the pile is firstly discretized into *n* elements, as shown in Figure 1. The value of the displacement at the bottom of the pile ρ_b^n is assumed for initiating the T-z analysis. Then the behavior of pile can be obtained by iterating the following calculations for each pile element starting from the n^{th} to the 1^{st}, and reaching convergence one by one. The axial forces at the base, middle and top of the i^{th} element are defined as follow:

(1)
$$Q_{b,M}^{i} = \begin{cases} Q_{t,M}^{i+1} & (i \neq n) \\ Q_{b,max} \cdot f_{Q-z}(\rho_b) & (i = n) \end{cases}$$

(2)
$$Q_{t,M}^{i} = 0$$

(3)
$$Q_{ave,M}^{i} = (Q_{b,M}^{i} + Q_{t,M}^{i})/2$$

Next, the elastic compression of element *n* (Δ_M^n) can be calculated by dividing the average force Q_{ave}^n by the stiffness K_f^n, as follows:

$$\Delta_M^i = Q_{ave,M}^i / K_f^i \quad (4)$$

Next, the displacement at the base, middle and top of i^{th} element are defined as follow:

$$\rho_{b,M}^i = \begin{cases} \rho_{t,M}^{i+1} & (i \neq n) \\ \rho_{b,M} & (i = n) \end{cases} \quad (5)$$

$$\rho_{s,M}^i = \rho_{b,M}^i + 0.5\Delta_M^i \quad (6)$$

$$\rho_{t,M}^i = \rho_{b,M}^i + \Delta_M^i \quad (7)$$

Next, the mobilized side shear force ($Q_{s,M}^n$) and new axial force ($Q_{t,M}^i$) at top can be defined as follows:

$$Q_{s,M}^i = Q_{s,max}^i \cdot f_{T-z}^{loading}(\rho_{s,M}^i) \quad (8)$$

$$Q_{t,M}^i = Q_{b,M}^n + Q_{s,M}^n \quad (9)$$

Then, Equations (3) to (9) are repeated in sequence until the absolute value of the change in $Q_{t,M}^i$ between different iterations becomes less than a user-specified criterion (a value of 10^{-10} is used in this study). After the i^{th} element converges, the same process used for the i^{th} element is used for the $(i\text{-}1)^{th}$ element, and so on. Once the 1^{st} element converges, Newton's method with a secant stiffness (k_{sec}) that passes through the origin is used to find the value of the base displacement ($\rho_{b,M}^i$) that causes the corresponding load on the top of the pile $Q_{t,M}^1$ to equal the applied mechanical load (P).

To extend the mechanical load transfer analysis to thermo-mechanical loading conditions, a spring should be added to the top of the pile that represents the pile head-structure stiffness (Knellwolf et al. 2011). When an energy pile is heated or cooled, it begins to expand or contract about its null point (Bourne-Webb et al. 2009) defined as the location in the pile where there is no thermal expansion or contraction, assuming that the temperature change occurs uniformly throughout the pile. The complexity of the algorithm for solving the behavior of energy pile is largely alleviated once the null point is identified, and the behavior of pile can be analyzed by separately investigating the parts of the pile below and above the null point.

To compute the settlement and the stress distribution of the energy pile under thermo-mechanical loading (restricted to heating in this study), the first step is to assume a null point location, NP. Then, the pile is evenly divided into n_1 elements for the part of the pile above NP and n_2 elements for the part of the pile below NP into, as shown in Figure 1. The mechanical load transfer analysis is performed and the displacements and forces on each element of the pile under mechanical loading are used as the initial condition for heating of the energy pile. After this preprocessing is done, the energy pile is initially assumed to be totally free to move similar to the approach of Knellwolf et al. (2011), in which case an initial estimate of the thermal elongations of each element can be obtained from the following expression:

$$\Delta_T^i = L^i \alpha_T \Delta T \tag{10}$$

For the part of energy pile below the null point, these elements move downward. Thus, the thermal displacement at the top, middle and base of element $(n_1 + 1)$ downward to element n can be calculated as follows:

$$\rho_{t,T}^i = \begin{cases} 0 & for\ i = n_1 + 1 \\ \rho_{b,T}^{i-1} & for\ i \neq NP \end{cases} \tag{11}$$

$$\rho_{s,T}^i = \rho_{t,T}^i + \frac{\Delta_T^i}{2} \tag{12}$$

$$\rho_{b,T}^i = \rho_{t,T}^i + \Delta_T^i \tag{13}$$

and the thermo-mechanical displacements can be calculating as follows:

$$\rho_{b,MT}^i = \rho_{b,M}^i + \rho_{b,T}^i \tag{14}$$

where the subscripts “T” and “MT” represent the thermal and combined thermal and mechanical loading, respectively.

Next, the thermo-mechanical force at base, side and top of elements from n upward to the element $(n_1 + 1)$ can be calculated using Equations (15) to (17), as follows:

$$Q_{b,MT}^{i} = \begin{cases} Q_{b,max} \cdot f_{Q-z}^{loading}\left(\rho_{b,MT}^{i}\right) & for\ i = N \\ Q_{t,MT}^{i+1} & for\ i \neq N \end{cases} \tag{15}$$

$$Q_{s,MT}^{i} = Q_{s,T,max}^{i} \cdot f_{T-z}^{loading}\left(\rho_{s,MT}^{i}\right) \tag{16}$$

$$Q_{t,MT}^{i} = Q_{s,MT}^{i} + Q_{b,MT}^{i} \tag{17}$$

and the thermally induced axial stress at the middle of each element can be calculated as follows:

$$\sigma_{T}^{i} = \frac{Q_{t,MT}^{i} + Q_{b,MT}^{i}}{2A_b} - \sigma_{M}^{i} \tag{18}$$

where σ_{M}^{i} is calculated as follows:

$$\sigma_{M}^{i} = \frac{Q_{ave,M}^{i}}{A_b} \tag{19}$$

After the forces acting on these elements are defined, the actual thermal elongation of each element is calculated as follows:

$$\Delta_{Tactual}^{i} = \Delta_{T}^{i} - \frac{\sigma_{T}^{i}.L_i}{E} \tag{20}$$

The actual thermal elongation of each element will be lower than that present when the energy pile is free to move. Equations (11) to (19) can then be recalculated using the thermal elongation from Equation (20) for the pile elements below the null point, and this process should be repeated until the values of restrained thermal elongation converge to a desired tolerance (i.e., when the difference between the new and old elongations calculated with Equation (20) is less than 10^{-10}). A similar process for solving for the behavior of the part of the energy pile below the null point can be applied for the part above the null point but instead considering the boundary conditions at the head of the pile. It should be noted that in the region of the pile above the null point, the pile will move upward and the side shear stress will decrease following the unloading path shown in Figure 2.

When both parts of the pile reach convergence, the unbalanced force at the null point can be defined as follows:

$$F_{unb} = \left|Q_{t,MT}^{NP+1}\right| - \left|Q_{b,MT}^{NP}\right| \tag{21}$$

If the unbalanced force F_{unb} is not less than a user-defined tolerance, this means that the assumed null point is not the actual one. If F_{unb} is positive, the actual null point is located at a lower point than the currently assumed null point, and a new null point needs to be assumed at a lower location. If F_{unb} is negative, the opposite is true. After a new null point is selected based on the sign of the unbalanced force, the process starting from pile discretization needs to be repeated. When the unbalanced force F_{unb} is less than the user-defined tolerance, the selected null point is approximately at the actual null point and the pile can be assumed to be in thermo-mechanical equilibrium.

Discussion of the T-z and Q-z Curves

The relationships between displacement and mobilized side shear resistance and toe resistance are defined using Equations (22) and (23), respectively:

$$Q_s^i = Q_{s,max}^i \cdot f_{T-z}\left(\rho_s^i\right) \tag{22}$$

$$Q_b = Q_{b,max} \cdot f_{Q-z}(\rho_b^n) \tag{23}$$

where $Q_{s,max}^i$ and $Q_{b,max}$ are ultimate side shear force and ultimate end bearing, respectively, and f_{T-z} and f_{Q-z} are normalized force values that depend on the displacement of the pile element and toe elements ρ_s^i and ρ_b^n, respectively. The relationships between f_{T-z} and f_{Q-z} and displacement are typically referred to as the T-z and Q-z curves, respectively, in axial load transfer analyses.

The ultimate side shear force for undrained or drained soils can be estimated using different methods depending on the soil type and the assumed effects of temperature on the surrounding soil. The former subject has been well-studied, and includes methods that assume a constant side shear with depth (typical for soil layers that are undrained during pile loading) or methods that assume the side shear increases with depth (typical for soil layers that are drained during pile loading, but can also be applied to soil layers that are undrained during pile loading). Consideration of the effects of temperature on the surrounding soil in a load transfer analysis is complex, and ideally requires a combination of heat transfer analyses (Loveridge and Powrie 2013), thermo-hydro-mechanical constitutive modeling (Laloui et al. 2015), and potential changes in stress state imposed on the soil by the differential thermal expansion of the pile and soil during heating (McCartney and Rosenberg 2011; Olgun et al. 2014b). Except in the case of normally consolidated clays, heating is expected to lead to thermo-elastic expansion of the soil in the zone of influence of the changes in temperature. Heating of the soils surrounding energy piles is likely to occur slowly. For example, Murphy and McCartney (2015) found that the temperature of a full-scale energy pile during building heating and cooling changed by approximately 20 °C over the course of 6 months. This rate of heating is expected to be slow enough to permit drainage of thermally-induced excess pore water pressures in the case that they occur, so drained heating analyses can be assumed. Nonetheless, due to a lack of experimental evidence on the impact of the thermo-hydro-mechanical response of soils surrounding energy piles, and because this study focuses on relatively stiff, non-plastic soils that are expected to behave thermo-elastically during heating, the impact of temperature change on the soil properties is neglected in the thermo-mechanical load-transfer analysis.

The following equation can be used to calculate the side shear capacity of soils that have constant undrained shear strength with depth (referred to generally here as undrained soils):

$$Q_{s,max}^{i} = \alpha A_{s}^{i} c_{u} \tag{24}$$

where α is an empirical reduction factor representing soil-interface behavior, and A_s^i is the pile surface area for the element of interest. The value of α in this equation varies with the undrained shear strength and soil layering (e.g., Tomlinson 1971), but may also vary with temperature depending on the impact of temperature on the soil. However, temperature effects on α were not considered in this study as more experimental evidence is required to support this and to ensure that temperature effects on α and c_u are appropriately isolated.

Alternatively, the β method can be used to estimate the side shear capacity of soils that have a shear strength increasing with depth (referred to generally here as drained soils, even though undrained soils may also have an increasing undrained shear strength with depth). The drained shear strength analysis here includes a feature to account for the potential change in lateral stress due to differential expansion of the pile and soil similar to the approach of McCartney and Rosenberg (2011), as follows:

$$Q_{s,T,max}^{i} = [c' + \beta_T \sigma_v'(z)] A_s^i \tag{25}$$

where c' is an apparent cohesion that can be used to evaluate the impact of unsaturated conditions on the interface shear strength (c' is assumed equal to zero for dry or saturated soils), and β_T is a temperature-dependent side shear factor that can be defined as follows:

$$\beta_T = \chi_T \left[K + \left(K_p - K\right) K_T\right] tan\phi' \tag{26}$$

where χ_T is a fitting parameter, K is the initial coefficient of lateral earth pressure before heating, K_p is the coefficient of passive lateral earth pressure, and K_T is a reduction factor representing the mobilization of passive earth pressure with thermal-induced strain, equal to:

$$K_T = \kappa \alpha_T \Delta T \left(\frac{D/2}{0.02L}\right) \tag{27}$$

where κ is an empirical coefficient representing the soil resistance to expansion of the pile, α_T is the coefficient of thermal expansion of reinforced concrete, and the geometric normalizing factor $[(D/2)/0.02L]$ was proposed by Reese et al. (2006). The value of κ may be a stress-dependent variable, but was assumed to be constant and equal to 65 based on centrifuge tests on Bonny silt performed by McCartney and Rosenberg (2011). The value of K assumed in the analysis depends on the soil type and drilled shaft construction method for the energy pile. It can be assumed that $K = K_0$ for piles in stiff soils or rock where the open-hole method is used, K is closer to K_a for piles in soft clay or sand. The value of K may be greater than K_0 in model experiments where the soil was placed using pluviation or compaction (e.g., Goode and McCartney 2015).

The ultimate end bearing $Q_{b,max}$ for the pile can be defined for different soils as follows:

$$Q_{b,max} = \begin{cases} A_b c_{u,b} N_c s_c d_c & \text{for undrained soil} \\ A_b \sigma'_{ZD} N_q & \text{for drained soil} \\ A_b q_u & \text{for rock or rigid materials} \end{cases} \tag{28}$$

where $c_{u,b}$ is the undrained shear strength of the soil or rock at the pile tip, A_b is the cross sectional area of the shaft toe, s_c is the shape factor (i.e., equal to 1.2 for a pile with a circular or square cross-section), d_c is the depth factor (i.e., equal to 1.5 for a pile with depth over diameter ratio larger than 2.5), N_c is the undrained bearing capacity factor for deep foundations (i.e., equal to 5 for a pile with a circular or square cross-section and a tip depth greater than 2 pile diameters), σ'_{ZD}

is vertical effective overburden, N_q is the bearing capacity factor related to effective friction angle obtained from Vesić (1975), and q_u is uniaxial compressive strength of rock. The last equation in Equation (28) is also used when simulating the behavior of model tests by Stewart and McCartney (2013) where an energy pile was placed on a rigid aluminum plate which can be assumed to have an extremely high value of q_u. Similar to the side shear capacity, heating of energy piles may lead to a change in end bearing capacity. Specifically, an energy pile is heated under a mechanical load (e.g., a building load), it is able to react against the building causing the soil at the toe to consolidate. This may lead to a higher end bearing capacity than a pile. Further research is needed to quantify this effect, and it is neglected in this study.

Examples of the Q-z and T-z curves for drilled shafts reported by O'Neill and Reese (1988) shown in Figure 2 are nonlinear, and have a shape that is approximately hyperbolic. Accordingly, they are represented in this study using a hyperbolic model for simplicity. The normalized side shear resistance (f_{T-z}) and normalized base reaction (f_{Q-z}) at any relative displacement are given by the following equations:

(29) $$f_{Q-z}(\rho_b^n) = \frac{\rho_b^n}{a_b + b_b \rho_b^n}$$

(30) $$f_{T-z}(\rho_s^i) = \begin{cases} \dfrac{\rho_s^i}{a_s + b_s \rho_s^i} & for\ loading \\ \dfrac{\rho_s^i}{a_s} + \dfrac{Q_{s,M}^i}{Q_{s,M,max}^i} - \left(\dfrac{1}{\dfrac{Q_{s,M,max}^i}{Q_{s,M}^i} - b_s} \right) & for\ unloading \end{cases}$$

where a_b and b_b are the parameters that determine the shape of the Q-z curve, a_s and b_s are parameters that determine the shape of the T-z curve, and $Q_{s,M}^i$ represents the side shear resistance force at a given depth in the pile after the mechanical load is applied (which is the initial condition for heating). Because Murphy and McCartney (2014) found that the T-z curves are not sensitive to temperature, the T-z curves evaluated in this study are assumed to be independent of temperature. The mobilized values of base reaction (Q_b^n) and the side shear resistance (Q_s^i) can be obtained from Equations (29) and (30) by multiplying them by the ultimate end bearing force at the tip or the ultimate side shear resistance force at a given depth in the pile, respectively.

This study uses the thermo-mechanical load transfer analysis described in the previous section to evaluate two scenarios: (i) a parametric analysis in which the side shear stress is assumed to be constant with depth (typical of a soil that is undrained during shearing) or in which it is assumed to increase with depth (typical of a soil that is drained during shearing, although this could also be applied to soils that are undrained during shearing if desired), and (ii) a calibration of the model with the information from real case studies. In the latter scenario, all of the soils investigated are assumed to have the case of an increasing shear strength with depth.

MODEL PARAMETRIC EVALUATION

Using the improved thermo-mechanical load transfer analysis, a parametric evaluation was performed to understand the roles of the different model parameters (i.e., the soil shear strength parameters, toe stiffness, head stiffness, side shear stress-displacement curve, and radial expansion) and other issues (i.e., magnitude of the temperature change). In order to assess the impact of each parameter, it was first important to come up with a baseline set of soil and pile properties and loading conditions. The pile was assumed to consist of the typical concrete mixture used in drilled shaft foundations in the field. The energy pile used for the baseline case has a length *L* of 13.1 m, a diameter *D* of 1.2 m, a unit weight of 24 kN/m^3, a Young's modulus *E* of 30 GPa, a head stiffness of 500 kN/mm and a coefficient of thermal expansion α_T of 10×10^{-6} m/(m°C). As semi-floating energy piles are the most common type of deep foundations encountered in practice, soil-structure interaction parameters representative of this type of pile are used for understanding the effect of each parameter, where a_s is 0.0035, a_b is 0.002, b_s and b_b are 0.9. These parameters are used in Equations (29) and (30), which are used to represent the smooth Q-z and T-z curves, respectively. A load of 500 kN is applied to the pile head then a uniform change in temperature of 20 °C with depth is applied. In all of the comparisons, it is assumed that the pile temperature is constant with depth, an assumption that is approximately valid based on field data (Murphy et al. 2015; Murphy and McCartney 2015).

The thermo-mechanical axial stresses and strains, mobilized side shear stresses, and thermo-mechanical displacements for energy pile under varying friction angle for energy piles in drained soils with an ultimate side shear capacity characterized by Equation (25) are shown in Figures 3(a) through 3(d). It is clear from the results in Figure 3(a) that the thermo-mechanical axial stresses increase with increasing friction angle. The results in Figure 3(b) show that the axial thermo-mechanical strains at the head decrease with increasing friction angle, while the results in Figure 3(c) show that the fiction angle does not affect the mobilized side shear stresses at the head of pile. The total and maximum negative side shear stress induced by heating increases and is applied to longer part of pile with an increase of friction angle as the tip capacity increases much more significant than side shear capacity. The results in Figure 3(d) indicate that the thermo-mechanical displacement at the tip decreases and the head of the pile moves upwards with an increase in drained friction angle, and the influence of drained friction angle on displacement diminishes for soils with a higher friction angle.

The maximum axial thermo-mechanical, thermal, mechanical stresses and pile thermo-mechanical, thermal, mechanical total axial strains (which is defined as the difference between the displacements of the pile head and pile tip, normalized by pile length) for varying friction angle values for energy pile in drained soils are shown in Figures 4(a) and 4(b). It can be observed from the results in Figure 4(a) that the thermo-mechanical axial stresses increase approximately linearly with an increase of friction angle ranging from 20 to 35°, and the largest thermo-mechanical axial stress is close to the head of pile. The results in Figure 4(b) show that the total pile expansion due to thermal and thermo-mechanical loading decreases with increasing friction angle. This is because the tip and side shear resistances increase with friction angle, leading to larger axial stresses to resist the pile expansion caused by heating.

The thermo-mechanical axial stresses and strains, mobilized side shear stresses, and thermo-mechanical displacements for an energy pile under varying undrained shear strength for energy pile in undrained soils with an ultimate side shear capacity described by Equation (24) are shown in Figures 5(a) through 5(d). It is clear from the results in Figure 5(a) that the axial thermo-mechanical stresses increase with increasing undrained shear strength, as expected. Figure 5(b) shows that the thermo-mechanical strains decrease with increasing undrained shear strength. As the undrained shear strength increases, the profiles of thermo-mechanical axial stresses and strains become increasingly nonlinear with depth. The axial thermo-mechanical strain decrease with increasing undrained shear strength, and the increase in undrained shear strength causes the null point to move downward and the thermo-mechanical stresses and strains to increase. The results in Figure 5(c) show a similar effect as that of the friction angle, where the total downward mobilized side shear stresses increase, and the total upward mobilized side shear stresses decrease with increasing undrained shear strength. The difference is that the increasing undrained shear strength leads to a greater increase in the downward mobilized side shear stresses at the head of the pile. The results in Figure 5(d) show that the thermo-mechanical displacement decreases with increasing undrained shear strength.

The maximum thermo-mechanical, thermal and mechanical axial stresses and the thermo-mechanical, thermal, mechanical total axial strains in undrained soils are shown in Figure 6. The maximum thermo-mechanical stresses in the pile in Figure 6(a) are observed to increase with an increase in undrained shear strength of soil, while the maximum mechanical stress is not sensitive to the undrained shear strength of the soil. The results in Figure 6(b) shows that the thermo-mechanical expansion decreases with increasing undrained shear strength, which occurs because an increase in undrained shear strength leads to an increase in both mobilized side shear stress and toe resistance, which serve to resist thermal expansion.

The effect of the magnitude of the change in temperature on the maximum values of axial stresses and total axial strains in terms of mechanical, thermal, and thermo-mechanical axial loading are shown in Figures 7(a) and 7(b), respectively. The results in both figures show that the maximum thermal and thermo-mechanical axial stresses and total axial strains increase approximately linearly with an increase of temperature. This is because the thermal expansion of the pile is linear and thermo-elastic, and the changes in temperature are not sufficient to reach the plastic portion of the T-z or Q-z curves for the axial loading case considered.

The effect of toe stiffness on maximum values of axial stresses and pile total strain in terms of mechanical, thermal, and thermo-mechanical values are shown in Figures 8(a) and 8(b), respectively. It can be observed from Figure 8(a) that the influence of a_b on the maximum thermal and thermo-mechanical axial stresses becomes less significant as a_b increases. This occurs because the initial stiffness of the mobilized base resistance Q-z curve decreases with increasing a_b, which leads to a softer base and allows more downward displacement. When there is less base resistance, the maximum axial stress decreases. A similar influence of toe stiffness on the trends in total axial strains can be observed in Figure 8(b).

The effect of head stiffness on maximum values of axial stresses and total axial strains in terms of mechanical, thermal, and thermo-mechanical values are shown in Figures 9(a) and 9(b). The results in both figures show that the maximum stresses and total axial strains increase with an increase in head stiffness, and the influence of K_h on the thermo-mechanical stresses and pile thermal expansions become less significant as K_h increases. This is because an increase in K_h lowers the uplift displacement by increasing the head resistance and larger side shear upward stress and toe resistance will be generated in order to achieve equilibrium, which leads to increases in axial stresses. As the head resistance stress increases, the null point moves upward and a larger part of the energy pile experiences a downward movement, which leads to an increase in the maximum displacements. Slightly larger axial stress on the top cause a lower maximum displacement by leading to a decrease in thermal expansion. When K_h is very large, the null point is very close to the head of pile. The uplift displacement at the pile head increases slightly despite the large changes in K_h. As the slope of the T-z curve and Q-z curve depends on the magnitude of displacement, in this case the axial displacements are insignificant so there is not a major effect of K_h on the axial stresses and strains.

The effect of the parameters of the side shear stress-displacement curve on the maximum values of axial stresses and total axial strains in terms of mechanical, thermal, and thermo-mechanical values are shown in Figures 10(a) and 10(b). The results in Figure 10(a) indicate that the maximum thermal and thermo-mechanical axial stress decreases with increases in a_s, and the influence of parameter a_s become insignificant when a_s is large. The results in Figure 10(b) indicate that an increase of parameter a_s leads to a slight increase of the total axial strains.

The effect of radial expansion on maximum values of axial stresses and total axial strains in terms of mechanical, thermal, and thermo-mechanical values are shown in Figures 11(a) and 11(b). The results in both Figures 11(a) and 11(b) indicate that radial expansion has a negligible influence on axial stresses and total axial strains. The results from this evaluation indicate that the effect of radial displacement is relatively small and can be neglected in the load transfer analysis, indicating that the trends in the load-settlement curves of McCartney and Rosenberg (2009) are more likely due to the effects of changing unsaturated conditions in the soil rather than radial expansion effects, although it is possible that the high initial lateral stresses induced by compaction in their tests may have had some effect on the stresses induced by lateral expansion.

MODEL CALIBRATION WITH FIELD/CENTRIFUGE DATA

The updated load-transfer model was calibrated to evaluate the expected soil-structure interaction response of four case studies, including one field study (Murphy et al. 2015) and three centrifuge studies (Stewart and McCartney 2013; Goode and McCartney 2015; Ng et al. 2014). The calibration of the model to these studies permits evaluation of the typical ranges of values of the different model parameters that are difficult to measure in the field, including the parameters of the T-z and Q-z curves fitting parameter χ_T and the head stiffness K_h. All of these studies involve non-plastic soils with a drained loading response and negligible temperature effects on the soil properties.

Case #1 Murphy et al. (2015)

In this study, several energy piles were constructed beneath a one-story, shower-shave building constructed at the US Air Force Academy (USAFA) beginning in March 2012. A site investigation was performed in September 2011, which consisted of two 102 mm-diameter borings located within the building footprint, extending 12 and 7 m below the ground surface. At selected intervals, disturbed samples were obtained by driving a split-spoon sampler. Exploration results from both boreholes were similar and showed three prominent strata, and relevant data are presented in Murphy et al. (2015). One of the end bearing concrete energy piles with a length of 15.2 m and a diameter of 0.61 m was considered in this evaluation (Foundation 4). The pile has a unit weight of 24 kN/m^3, a Young's modulus of 30 GPa, and a coefficient of thermal expansion is 12×10^{-6} m/m°C, and the empirical coefficient for radial expansion is assumed to be 65. An axial mechanical load of 833 kN was applied to the pile before changes of temperature of ΔT = 6, 12, 19°C were applied to heat the pile. For simplicity, the subsurface stiff gravel and sandstone layers are assumed to be one equivalent layer with a friction angle of 43.6° and a unit weight of 19.2 kN/m^3. An uniaxial compressive strength at the toe q_u of 12000 kPa was assumed for the intact sandstone at the toe. The calibrated load transfer parameters that provided the best fit to the data are: a_b = 0.002 and b_b = 0.9 for Q-z curve, a_s = 0.0003, b_s = 0.9, β = 0.9 for the T-z curve, fitting parameter χ_T = 2.5 and head stiffness K_h of 900 kN/mm.

The processed field data and simulation results for Foundation 4 are shown in Figure 12.The calibrated results in Figure 12 indicate a good estimate of the energy pile response in terms of the axial compressive stresses and strains and displacements induced by heating. Although the overall trend from the model is consistent with the field data, inconsistencies are observed for depths between 0 to 3 m, possibly because the model assumes a homogeneous layer of soil.

Case #2 Goode and McCartney (2015)

In this study, a scale-model semi-floating concrete energy pile having a diameter of 63.5 mm and a length of 342.9 mm (short pile) was heated in Bonny silt and Nevada sand, respectively, at a centrifuge g-level of 24 under an applied axial stress of 360 kPa. The corresponding prototype-scale energy pile has a diameter of 1.5 m and a length of 8.2 m, a unit weight of 24 kN/m^3, a

Young's modulus of 33 GPa, a coefficient of thermal expansion 16×10^{-6} m/m°C, and no head-structure restraint. The friction angles for Nevada sand and Bonny silt tested in this study are 35° and 32.4°, respectively, and the unit weight for Nevada sand and for Bonny silt are 14.8 and 17.9 kN/m^3, respectively. Because the Bonny silt was tested in unsaturated conditions, an apparent cohesion c' of 30 kPa was assumed for the particular compaction conditions. The empirical coefficient for radial expansion is assumed to be 65 based on the study of McCartney and Rosenberg (2010), although this parameter is not expected to have a major effect on the simulations. The calibrated parameters that provided the best fit to the data are: a_b = 0.006 and b_b = 0.9 for Q-z curve, a_s = 0.0002, b_s = 0.9, for the T-z curve and fitting parameter χ_T = 2.5 for Nevada sand; and a_b = 0.009 and b_b = 0.9 for Q-z curve, a_s = 0.0002, b_s = 0.9, for the T-z curve, fitting parameter χ_T = 2.5.

The comparisons of the calibrated model results with the experimental data for Nevada sand and Bonny silt are shown in Figures 13 and 14, respectively. Goode and McCartney (2015) plotted the thermal axial displacement values against the location at the midpoint between two strain gages. However, this should be plotted against the location of the upper gage so the experimental data from Goode and McCartney (2015) were re-analyzed so that the calculated thermal axial displacement values correspond to the location of the upper gage. The results shown in these figures indicate a good match between the overall trend of axial stresses and strains induced by thermal loading in this case study. The difference between the trends in the thermal strain and stress are probably due to the small differences between the average temperatures applied in the model from the actual temperature profile in the experiment, which was not completely uniform.

Case #3 Stewart and McCartney (2014)

In this study, a small-scale, end-bearing concrete model energy pile with dimensions of 50.8 mm in diameter and 533.4 mm in length was heated in a layer of unsaturated Bonny silt in the centrifuge at a g-level of 24.6 under an applied axial stress of 443 kPa. The corresponding prototype-scale energy pile has a length of 12.8 m and a diameter of 1.22 m, with a unit weight of 24 kN/m^3, a Young's modulus of 7.17 GPa, a coefficient of thermal expansion 7.5×10^{-6} m/m°C, and no head-structure restraint. The empirical coefficient for radial expansion is assumed to be 65. The friction angle used in this case is 32.4° and dry weight of soil is 16.9 kN/m^3. For this case, the unsaturated Bonny silt was found to have an apparent cohesion c' of 30 kPa. A mechanical load of 443 kN was applied to the pile head before heating in load-control conditions. A uniaxial compressive strength at the toe q_u of 25000 kPa was used in the analysis as the toe of the pile is supported by a relatively rigid aluminum plate. The calibrated parameters that provided the best fit for the data are: a_b = 0.002 and b_b = 0.9 for Q-z curve, a_s = 0.0008, b_s = 0.9, for the T-z curve, fitting parameter χ_T = 2.5.

The predicted axial compressive stress profiles using load-transfer model analysis along with the centrifuge data for each temperature change condition are shown in Figures 15(a) through 15(c). Stewart and McCartney (2014) plotted the thermal axial displacement values against the location at the midpoint between two strain gages. However, this should be plotted against the location of the upper gage so the experimental data from Stewart and McCartney were re-analyzed so that the calculated thermal axial displacement values correspond to the location of the upper gage. A good match was observed between the calibrated and measured data in Figures 15(a) through 15(c). The worst fit was observed near the head of the pile for small changes in temperature, likely due to differences between the average pile temperature and the actual pile temperature at that depth.

Case #4 Ng et al. (2015)

In this study, three instrumented, semi-floating aluminum alloy model pipe piles having an external diameter of 22 mm and length of 600 mm were tested in saturated sand at a centrifuge g-level of 40. The corresponding prototype-scale energy pile has a length of 19.6 m, a diameter of 0.88 m, a Young's modulus of 70 GPa and a coefficient of thermal expansion of 22.2×10^{-6} m/(m·K). No head-structure restraint or mechanical load was applied at the head of piles. The empirical coefficient for radial expansion is assumed to be 65, despite the difference in materials from the previous studies, due to the lack of strong effect of this variable. All the tests were carried out in saturated Toyoura sand with a buoyant unit weight γ = 9.4 kN/m^3 and a friction angle of 31°.

The calibrated parameters that provided the best fit for the data are: a_b = 0.07 and b_b = 0.9 for the Q-z curve, and a_s = 0.006, b_s = 0.9 for the T-z curve. The fitting parameter χ_T is assumed to be 1, since the coefficient of friction of aluminum with sand is more than half that of concrete and sand. The predicted thermal induced axial force profiles obtained using load-transfer model analysis along with the experimental data for different changes in temperature are shown in Figure 16. The load transfer results are generally consistent with the centrifuge data, although there are discrepancies in the region around the null point. The trends in the experimental data with depth in this study were more nonlinear than those observed in the other studies, with a lower null point. This could be due to the characteristics of the pile or uncertainties in the nonlinearity of the pile-sand interface shear resistance.

Case Study Summary

A summary of the model parameters from the four different studies is presented in Table 1. The sands and sandstone were both represented using drained shear strength analyses, while the silt was represented using an undrained analysis with a linear distribution with depth, with the ultimate side shear distribution with depth described by Equation (25) for all of the soils. The end bearing resistance was modeled depending on the corresponding end bearing condition. The differences in the model parameters for the Bonny silt layers tested by Stewart and McCartney (2014) and Goode and McCartney (2015) can be attributed to the different compaction conditions for the soil layers tested. The value χ_T was found to be highly affected by the type of material and roughness on the side of the pile. The energy piles in the centrifuge were installed by placing the soil around the piles, which may have led to different interface shear strengths from those expected of a full-scale pile in the field.

DESIGN EVALUATION CHARTS

Soil-Structure Interaction Curves

The Q-z curves and T-z curves used in the simulation of the different case histories with the parameters listed in Table 1 are compared in Figures 17(a) and 17(b), respectively. Although there is some spread in the curves depending on the stiffness of the soil and the constraint provided at the base of the pile, the curves all fall within a reasonable band. The data points for the mobilized toe resistance and displacement values for changes in temperature of 10 and 20 °C are shown on top of the curves in Figure 17(a) for comparison. In most of the cases the normalized tip resistance value does not exceed 0.3 and falls in the linear range of the Q-z curve. Accordingly, it is fair to consider the Q-z curve to be linear for simplifying the computation in practice. It can be observed from Figure 17(b) that the mobilized side shear stress reaches an ultimate value at low displacements. Accordingly, it is important to carefully consider ultimate side shear capacity for a given energy pile in design as this can affect the nonlinearity of trends with depth. The curves used to represent the behavior of the aluminum pile in sand tested by Ng et al. (2015) are softer than the other curves, potentially due to the loose sand and the smoother interface of the aluminum pile.

Ratios of the Mobilized Resistance to the Ultimate Resistance

A plot of the variations in the ratio of the total thermo-mechanical mobilized resistance to the ultimate resistance for the pile base resistance $Q_{b,MT}$ /$Q_{b,max}$ and the side shear resistance $Q_{s,MT}$/$Q_{s,max}$ are shown in Figure 18. For each of the case histories, $Q_{b,MT}$ is obtained by performing the thermo-mechanical load transfer analysis using calibrated parameters presented in Table 1, except the head stiffness K_h are varying from 0 to 1000 MN/m. The value of $Q_{s,MT}$ was obtained by summing the side shear resistances of each pile element from the simulation results, while the value of $Q_{b,max}$ was calculated using Equation (28). The value of $Q_{s,max}$ is calculated by summing the ultimate side shear force for each elements using Equation (25). Upward and downward resistances are taken as positive and negative, respectively.

During heating, the base resistance systematically increases. As observed in Figure 18, the value of $Q_{b,MT}$ /$Q_{b,max}$ increases by an insignificant compared to increase in the value of $Q_{s,MT}$ /$Q_{s,max}$ as the head stiffness K_h is varied from 0 to 1000 MN/m. The value of $Q_{s,T}$ /$Q_{s,max}$ increases linearly with the value of $Q_{b,T}$ /$Q_{b,max}$ for each case with a slope in the range of 8 to 50 depending on the stiffness of the soil-pile interface. The head stiffness has a significant influence on the side shear resistance caused by heating. It is clear that the aluminum pile tested by Ng et al. (2015) showed the most nonlinearity and widest mobilization ratios in all of the cases studied due to the higher coefficient of thermal expansion of the pile and the comparably softer load transfer curves. The thermo-mechanical stresses are closer to failure (i.e., ratios closer to 1.0). More nonlinear behavior in the side shear resistance is observed as the head stiffness increases, leading to larger downward displacements of the pile. It should be noted that it is increasingly possible that creep strains or cyclic effects may be encountered for piles loaded closer to failure (Pasten and Santamarina 2014).

Load-Settlement Relationships for the Head of the Energy Pile

It is important to understand the variation of head displacement for design because if it is more than an allowable limit for the structure, then the structure may fail by the "Serviceability Limit State". The variations in head settlement ($\rho_{t,T}$) and head load ($Q_{t,T}$) induced by temperature variations for different head stiffness values are presented in Figure 19. Downward head load and head settlement are taken as positive. The values of $\rho_{t,T}$ and $Q_{t,T}$ in Figure 19 are obtained from thermo-mechanical load transfer analysis using parameters presented in Table 1 with stiffness K_h varying from 0 to 1000 MN/m. An interesting observation is that most of the curves for the piles made of concrete have a similar slope, which may be affected by the magnitudes of the Young's modulus and coefficient of thermal expansion of the pile, as well as the shapes of the T-z and Q-z curves. This plot is useful to assess the maximum thermal axial stress and displacement at the head of an energy pile made from a given material. It also emphasizes that very stiff pile elements with high thermal expansion (i.e., aluminum) may have different behavior than softer pile elements with lower thermal expansion (i.e., concrete).

CONCLUSIONS

This study involved the development of a thermo-mechanical load-transfer analysis for capturing the behavior of energy piles during mechanical loading and monotonic heating. The key for successful simulation was found to be an accurate identification of the null point location. Once the null point was identified, the status of axial strain and stress in the energy pile were iteratively computed to reach equilibrium in the upper and lower parts of the pile considering compatibility of displacements between the soil and pile. A parametric evaluation was performed to identify the effects of different parameters on the axial stress and strain distributions within the pile and the total axial strain computed from the displacements at the head and toe of the pile. The model for the ultimate side shear capacity used in the analysis was found to affect the behavior of the energy pile by affecting the ultimate capacity and the mobilized side shear stress distribution at different depth. The increasing changes in temperature caused the energy pile to expand resulting in larger resistance to movement at the heat, toe and sides of the pile, leading to increases in axial stress in the pile. The temperature had a linear effect on the maximum axial stress in the pile for the range of temperatures investigated. The toe stiffness mainly affects the displacements at the ends of the pile and the magnitude of the axial stress near the toe of the pile. The head stiffness leads to greater downward toe displacements as well as greater stresses along the pile due to the greater mobilization of the end bearing resistance. The impact of the side shear stress-displacement curve mainly lies in the thermally-induced stress distribution along the pile. The radial expansion was found to cause a slight increase in side shear capacity, but this effect was small enough to be neglected.

The thermo-mechanical load-transfer model was calibrated using the results from four case studies involving energy piles in non-plastic soils or rock in order to evaluate the typical ranges of values of the model parameters. The calibrated results were synthesized to provide preliminary design charts in terms of the ratio of the mobilized resistance to the ultimate resistance and the head load and head settlement. However, the evaluation of more case studies need to be evaluated using the load transfer analysis to fully delineate these trends.

Issues that require further evaluation using the load transfer method include the impacts of thermal volume change of the surrounding soil or rock on the changes in ultimate side shear and end bearing capacities and shapes of the T-z and Q-z curves. As this study was focused on non-plastic soils, the effect of this issue was assumed to be insignificant. However, energy piles may be installed in soft clays or expansive clays were appreciable volume changes or cyclic effects may be encountered in the soil leading to changes in the ultimate side shear or end bearing values. Another issue that deserves further study is the role of heating and cooling superimposed atop an initial force-displacement condition induced by mechanical loading. This requires modifying the shapes for the nonlinear Q-z and T-z curves to capture the hysteretic heating and cooling trends. Although this has been considered in other studies for elastic-perfectly plastic models, this modification is still required for the hyperbolic curves used in this study. Although the hyperbolic model can be used to form a backbone curve in the directions of monotonic heating and cooling, a transition function is required to extend the unloading path from the point of zero stress to the backbone curve in the other direction of displacement, which will require additional experimental validation.

ACKNOWLEDGMENTS

Financial support from NSF grant CMMI-0928159 is gratefully acknowledged. The contents of this paper reflect the views of the authors and do not necessarily reflect the views of the sponsor.

REFERENCES

Akrouch, G., Sanchez, M., and Briaud, J.L. (2014). "Thermo-mechanical behavior of energy piles in high plasticity clays." Acta Geotechnica. 9(3), 399-412.

Amatya, B. L., Soga, K., Bourne-Webb, P. J., Amis, T., and Laloui, L. (2012). “Thermo-mechanical behaviour of energy piles.” Géotechnique, 62(6), 503–519.

Bouazza, A., Singh, R.M., Wang, B., Barry-Macaulay, D., Haberfield, C., Chapman, G., Baycan, S., and Carden, Y. (2011). "Harnessing on site renewable energy through pile foundations." Aust. Geomech. J., 46(4), 79–90.

Bourne-Webb, P., Amatya, B., Soga, K., Amis, T., Davidson, C. and Payne, P. (2009). "Energy pile test at Lambeth College, London: Geotechnical and thermodynamic aspects of pile response to heat cycles." Géotechnique 59(3), 237–248.

Brandl, H. (2006). "Energy foundations and other energy ground structures." Géotechnique. 56(2), 81-122.

Burger, A., Recordon, E., Bovet, D., Cotton, L. and Saugy, B. (1985). Thermique des Nappes Souterraines. Laussane: Presses Polytechniques Romandes.

Burlon, S., Habert, J., Szymkievicz, F., Suryatriyastuti, M., and Mroueh, H. (2013). "Towards a design approach of bearing capacity of thermoactive piles." European Geothermal Congress 2013, Pisa, Italy. pp. 1-6.

Coyle, H.M., and Reese, L.C. (1966). "Load transfer for axially loaded piles in clay." J. Soil Mech. and Found. Div., 92(2), 1–26.

Goode, J.C., III and McCartney, J.S. (2014). "Evaluation of head restraint effects on energy foundations." Proceedings of GeoCongress 2014 (GSP 234), M. Abu-Farsakh and L. Hoyos, eds. ASCE. pp. 2685-2694.

Goode, J.C., III and McCartney, J.S. (2015). "Centrifuge modeling of boundary restraint effects in energy foundations." Journal of Geotechnical and Geoenvironmental Engineering. 141(8), 04015034-1-04015034-13. DOI: 10.1061/(ASCE)GT.1943-5606.0001333.

Goode, J.C., III, Zhang, M. and McCartney, J.S. (2014). "Centrifuge modeling of energy foundations in sand." Physical Modeling in Geotechnics: Proceedings of the 8th International

Conference on Physical Modelling in Geotechnics. Perth. Jan. 14-17. C. Gaudin and D. White, eds. Taylor and Francis. London. pp. 729-736.

Knellwolf, C., Peron, H., and Laloui, L. (2011). “Geotechnical analysis of heat exchanger piles.” Journal of Geotechnical and Geoenvironmental Engineering. ASCE. 137(12), 890-902.

Laloui, L. (2011). “In-situ testing of heat exchanger pile.” Proc., GeoFrontiers 2011, J. Han and D. E. Alzamora, eds., ASCE, Reston, VA, 410–419.

Laloui L, Moreni M, Vulliet L. (2003). “Comportement d'un pieu bi-fonction, fondation et échangeur de chaleur.” Canadian Geotechnical Journal 40(2): 388–402.

Laloui, N. and Nuth, M. (2006). “Numerical modeling of some features of heat exchanger pile.” ASCE GSP 153. ASCE. Reston, VA. pp. 189-195.

Laloui, L., Nuth, M., and Vulliet, L. (2006). “Experimental and numerical investigations of the behaviour of a heat exchanger pile.” International Journal of Numerical and Analytical Methods in Geomechanics. 30(8), 763–781.

Laloui, L., Olgun, C.G., Sutman, M., McCartney, J.S., Coccia, C.J.R., Abuel-Naga, H.M., and Bowers, G.A. (2014). “Issues involved with thermo-active geotechnical systems: Characterization of thermo-mechanical soil behavior and soil-structure interface behavior.” The Journal of the Deep Foundations Institute. 8(2), 107-119.

Loveridge, F., Powrie, W. (2013). “Temperature response function (G-functions) for single pile heat exchangers.” Energy. 57, 554–564.

McCartney, J.S. (2015). “Structural performance of thermo-active foundations.” In: Advances in Thermo-Active Foundations. M. Krarti, ed. ASME Press. New York. pp. 1-44. ISBN: 9780791861059.

McCartney, J. S. and Rosenberg, J. E. (2011). "Impact of heat exchange on side shear in thermo-active foundations." ASCE Geo-Frontiers, 488-498.

McCartney, J.S., and Murphy, K.D. (2012). "Strain distributions in full scale energy foundations." DFI Journal. 6(2), 28–36.

Mimouni T, Laloui L. (2014). "Towards a secure basis for the design of geothermal piles." Acta Geotechnica 9(3): 355-366.

Murphy, K.D., McCartney, J.S., and Henry, K.S. (2015). "Evaluation of thermo-mechanical and thermal behavior of full-scale energy foundations." Acta Geotechnica. 10(2), 179-195.

Murphy, K.D. and McCartney, J.S. (2014). "Thermal borehole shear device." ASTM Geotechnical Journal. 37(6), 1040-1055.

Murphy, K.D. and McCartney, J.S. (2015). "Seasonal response of energy foundations during building operation." Geotechnical and Geological Engineering. 33(2), 343-356.

Ng, C.W.W., Shi, C., Gunawan, A. & Laloui, L. (2014). "Centrifuge modelling of energy piles subjected to heating and cooling cycles in clay." Géotechnique Letters. 4, 310-316.

Ng, C.W.W., Shi, C., Gunawan, A., Laloui, L. (2015). "Centrifuge modelling of heating effects on energy pile performance in saturated sand." Canadian Geotechnical J. 52, 1-13.

Olgun, C.G., Ozudogru, T.Y., Abdelaziz, S.L., and Senol, A. (2014a). "Long-term performance of heat exchanger pile groups." Acta Geotechnica. 10(5), 553-569.

Olgun, C., Ozudogru, T., and Arson, C. (2014b). "Thermo-mechanical radial expansion of heat exchanger piles and possible effects on contact pressures at pile–soil interface." Géotechnique Letters, 10.1680/geolett.14.00018, 170-178.

Ouyang, Y., Soga, K., and Leung, Y. F. (2011). “Numerical back-analysis of energy pile test at Lambeth College, London.” Proc., Geo-Frontiers 2011 (GSP 211), J. Han and D. E. Alzamora, eds., ASCE, Reston, VA, 440–449.

Ozudogru, T.Y., Olgun, C.G. and Senol, A. (2014). “3D numerical modeling of vertical geothermal heat exchangers.” Geothermics. 51, 312–324.

Pasten, C. and Santamarina, J.C. (2014). “Thermally induced long-term displacement of thermoactive piles.” J. Geotech. Geoenviron. Eng. 140(5), 06014003.

Plaseied, N. (2012). Load Transfer Analysis of Energy Foundations. MS Thesis. University of Colorado Boulder.

Reese, L.C., O’Neill, M.W. (1987), “Drilled shafts: construction procedures and design methods.” Report FHWA-HI-88-042, US Department of Transportation, Federal Highway Administration, Office of Implementation, McLean, Virginia.

Reese, L.C., Isenhower, W.M. and Wang, S.-T. (2006). Analysis and Design of Shallow and Deep Foundations. Wiley Interscience. New York.

Rollins, K.M., Clayton, R.J., and Mikesell, R.C. (1997). “Ultimate side friction of drilled shafts in gravel.” Foundation Drilling, June/July, pp. 10-13.

Rotta Loria, A.F., Gunawan, A., Shi, C., Laloui, L. & Ng, C.W.W. (2015a). “Numerical modelling of energy piles in saturated sand subjected to thermo-mechanical loads.” Geomechanics for Energy and the Environment 1, Vol. 1, 1-15.

Rotta Loria, A., Donna, A., and Laloui, L. (2015b). “Numerical study on the suitability of centrifuge testing for capturing the thermal-induced mechanical behavior of energy piles.” J. Geotech. Geoenviron. Eng. 10.1061/(ASCE)GT.1943-5606.0001318, 04015042.

Stewart, M.A. and McCartney, J.S. (2014). “Centrifuge modeling of soil-structure interaction in energy foundations.” J. Geotech. Geoenviron. Eng. 140(4), 04013044-1-04013044-11.

Suryatriyastuti M.E., Mroueh H., Burlon S. and Habert J. (2013). Numerical analysis of the bearing capacity in thermo-active piles under cyclic axial loading. Energy Geostructures: Innovation in Underground Engineering. L. Laloui and A. Di Donna. Hoboken, ISTE Ltd. and John Wiley and Sons: 139-154.

Sutman, M., Brettmann, T. and Olgun, C.G. (2014). “Thermo-mechanical behavior of energy piles: full-scale field test verification”. DFI 39th Annual Conference on Deep Foundations, Atlanta, GA. October 21-24, 2014. pp. 1-11.

Tomlinson, M.J. (1957). “The adhesion of piles in clay soils.” Proc., Fourth Intern. Conf. on Soil Mech. and Found. Engr. Vol. 2, pp. 66-71.

Vesić, A. (1975). “Bearing capacity of shallow foundations.” Foundation Engineering Handbook. 1st Ed. Winterkorn, H.F. and Fang, H.Y., eds. Van Nostrand Reinhold, New York.

Wang, B., Bouazza, A., Singh, R., Haberfield, C., Barry-Macaulay, D., and Baycan, S. (2014). “Post-temperature effects on shaft capacity of a full-scale geothermal energy pile.” J. Geotech. Geoenviron. Eng., 10.1061/(ASCE)GT.1943-5606.0001266, 04014125.

Wang, W., Regueiro, R., Stewart, M. A., and McCartney, J. S. (2012). “Coupled thermo-poro-mechanical finite element analysis of a heated single pile centrifuge experiment in saturated silt.” Proc., GeoCongress 2012 (GSP 225), R. D. Hryciw, A. Athanasopoulos-Zekkos, and N. Yesiller, eds., ASCE, Reston, VA, 4406–4415.

Wang, W., Regueiro, R., and McCartney, J. S. (2015). “Coupled axisymmetric thermo-poro-elasto-plastic finite element analysis of energy foundation centrifuge experiments in partially saturated silt.” Geotech. Geolog. Eng., 33(2), 373–388.

LIST OF FIGURE CAPTIONS

FIG. 1: Typical foundation schematic highlighting the location of the null point

FIG. 2: Typical nonlinear spring inputs and hyperbolic approximation for the load transfer analysis: (a) Q-z curve; (b) T-z curve

FIG. 3: Soil-structure interaction behavior of a semi-floating energy pile in drained soils: (a) Thermo-mechanical axial stresses; (b) Thermo-mechanical axial strains; (c) Mobilized side shear stresses; (d) Thermo-mechanical displacements

FIG. 4: Soil-structure interaction behavior of a semi-floating energy pile in drained soils: (a) Maximum stresses vs. ϕ; (b) Pile total axial strains vs. ϕ

FIG. 5: Soil-structure interaction behavior of a semi-floating energy pile in undrained soils: (a) Thermo-mechanical axial stresses; (b) Thermo-mechanical axial strains; (c) Thermal axial stresses; (d) Thermal axial strains

FIG. 6: Soil-structure interaction behavior of a semi-floating energy pile in undrained soils: (a) Maximum stresses vs. c_u; (b) Pile total axial strains vs. c_u

FIG. 7: Comparison of the impact of average pile temperature on soil-structure interaction behavior: (a) Maximum stresses vs. temperature; (b) Pile total axial strains vs. temperature

FIG. 8: Comparison of the impact of toe stiffness on soil-structure interaction behavior: (a) Maximum stresses vs. a_b; (b) Pile total axial strains vs. a_b

FIG. 9: Comparison of the impact of head stiffness on soil-structure interaction behavior: (a) Maximum stresses vs. K_h; (b) Pile total axial strains vs. K_h

FIG. 10: Comparison of the impact of T-z curve on soil-structure interaction: (a) Maximum stresses vs. a_s; (b) Pile total axial strains vs. a_s

FIG. 11: Comparison of the impact of radial expansion on soil-structure interaction: (a) Maximum stresses vs. κ; (b) Pile total axial strains vs. κ

FIG. 12: Simulated profiles of end bearing energy pile #4 with field test data by Murphy et al. (2015): (a) Thermal axial strains; (b) Thermal axial stresses; (c) Thermal axial displacements

FIG. 13: Simulated profiles of semi-floating energy pile with centrifuge model test data in Nevada sand by Goode and McCartney (2015): (b) Thermal axial strains; (d) Thermal axial displacements; (f) Thermal axial stress

FIG. 14: Simulated profiles of semi-floating energy pile with centrifuge model test data in Bonny silt by Goode and McCartney (2015): (a) Thermal axial strains; (b) Thermal axial displacements; (c) Thermal axial stress

FIG. 15: Simulated profiles of end-bearing pile with centrifuge model test data by Stewart and McCartney (2014): (a) Thermal axial strains; (b) Thermal axial displacements; (c) Thermal axial stress

FIG. 16: Simulated profiles of thermal axial forces for the semi-floating pile tested by Ng et al. (2015)

FIG. 17: Ranges in nonlinear spring inputs for the load transfer analysis obtained from the evaluation of the case studies: (a) Q-z curves; (b) T-z curves

FIG. 18: Ratios of $Q_{b,MT}/Q_{b,max}$ and $Q_{s,MT}/Q_{s,max}$ for different head restraint conditions and changes in temperature of $\Delta T = 20°C$

FIG. 19: Head resistance vs. head displacement plots at equilibrium for piles under a change in temperature of $\Delta T = 20°C$

TABLE 1: Summary of model parameters for different energy piles reported in the literature

		Murphy et al. (2015)	Goode and McCartney (2015)		Stewart and McCartney (2014)	Ng et al. (2015)
Soil Type		Sand	Nevada Sand	Bonny Silt	Bonny silt	Toyoura Sand
Foundation Type		Concrete	Concrete	Concrete	Concrete	Aluminum
L	(m)	15.2	8.2	8.2	12.8	19.6
D	(m)	0.61	1.5	1.5	1.22	0.88
α_T	($\mu\varepsilon$/°C)	-12	-16	-16	-7.5	-22
E	(GPa)	30	33	33	7.17	70
K_h	(kN/mm)	900	-	-	-	-
P	(kN)	833	360	360	443	-
γ	(kN/m^3)	19.2	14.2	17.9	17.9	9.4
ϕ'	(°)	43.6	35.0	32.4	32.4	31
N_q		–	33	24	–	21
q_u	(kPa)	12000	-	-	25000	
c'	(kPa)	-	-	30	30	-
χ_T		2.5	2.5	2.5	2.5	1
a_s		0.0003	0.0002	0.0002	0.0008	0.006
a_b		0.002	0. 006	0.009	0.002	0.07
b_s		0.9	0.9	0.9	0.9	0.9
b_b		0.9	0.9	0.9	0.9	0.9

*This model pile was end bearing on a rigid aluminum plate, so this was modeled as rock

Figure 1

Click here to download Figure Figure 1.tif

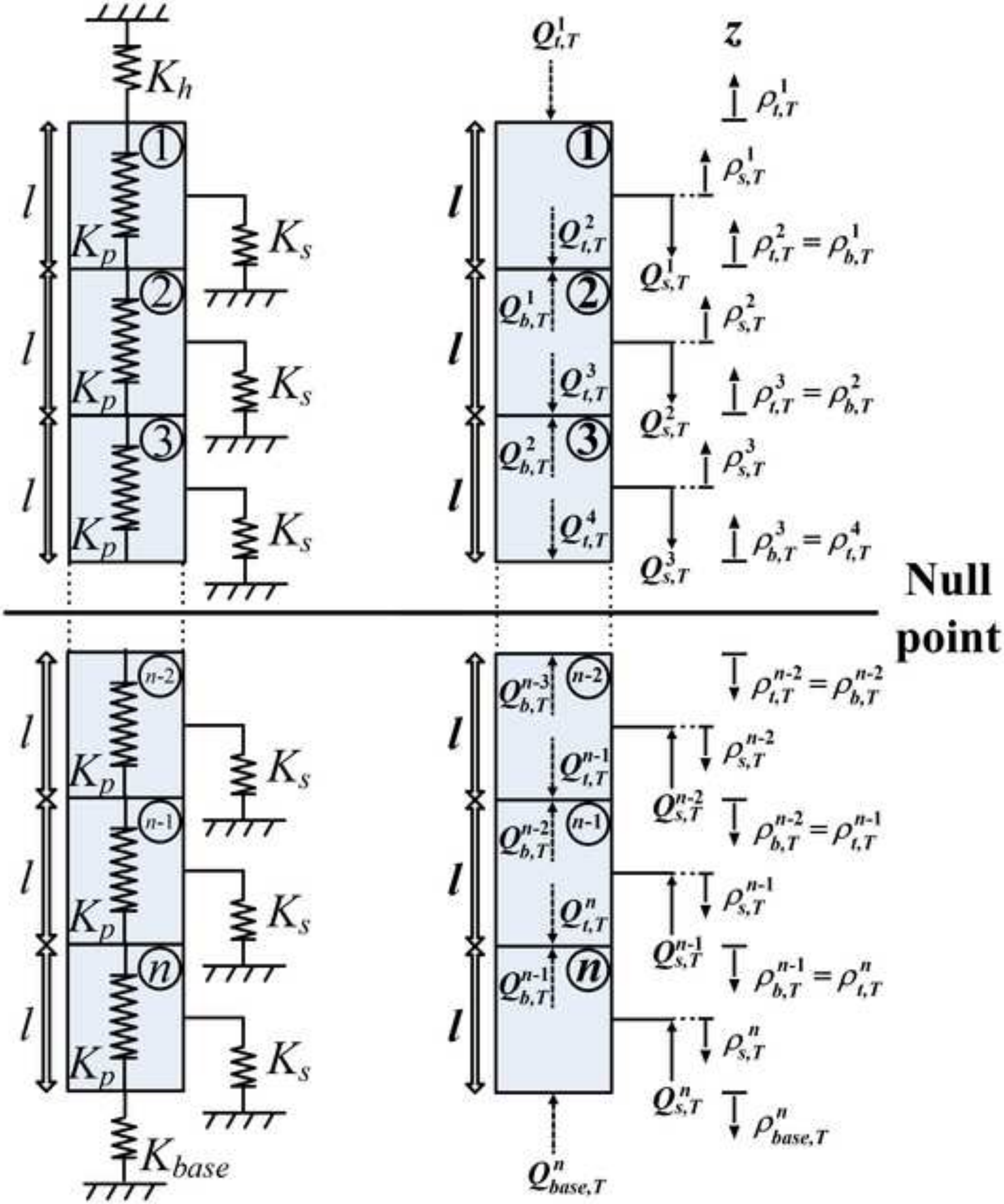

Figure 2

Click here to download Figure Figure 2.tif

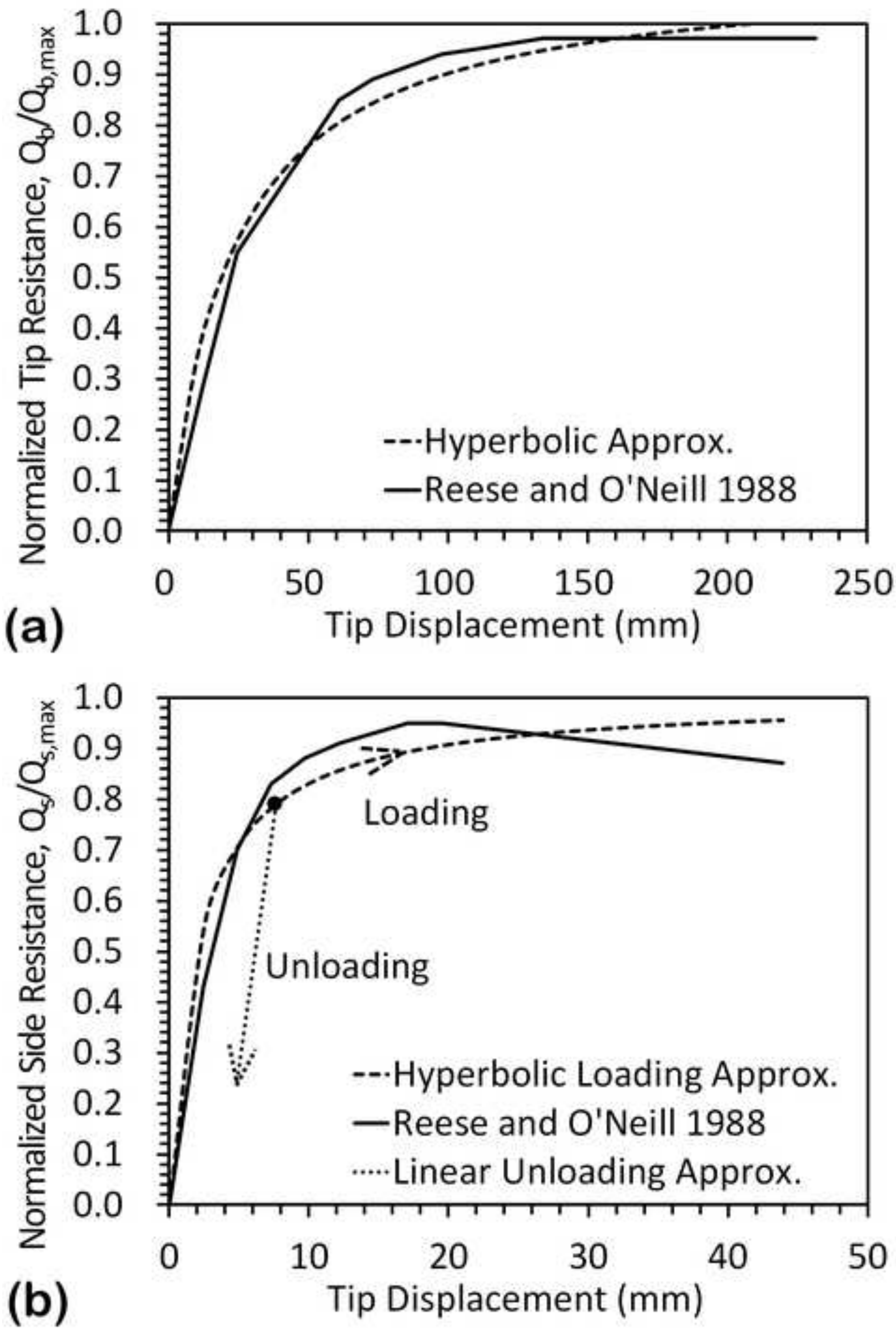

Figure 3

Click here to download Figure Figure 3.tif

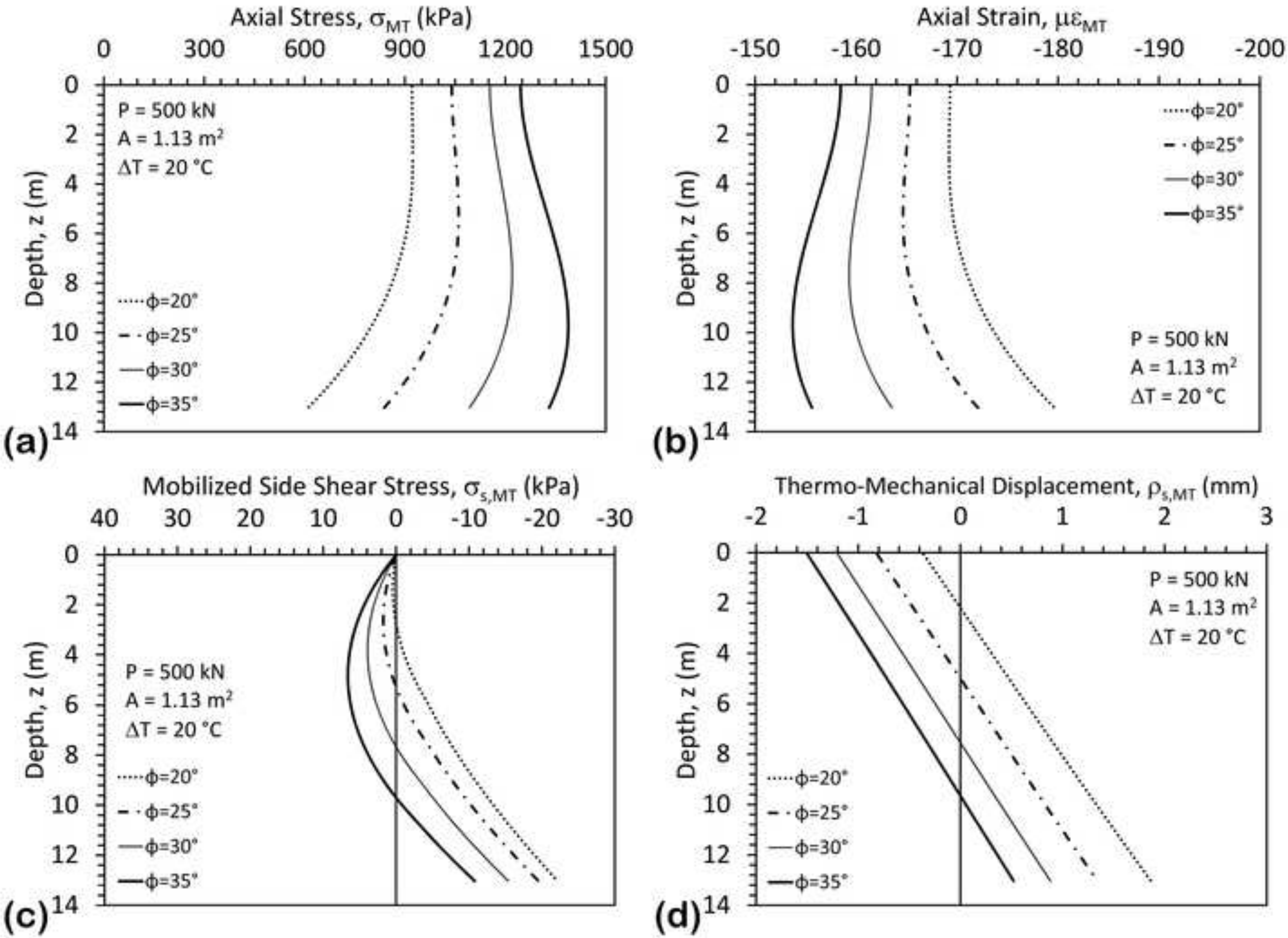

Figure 4 Click here to download Figure Figure 4.tif

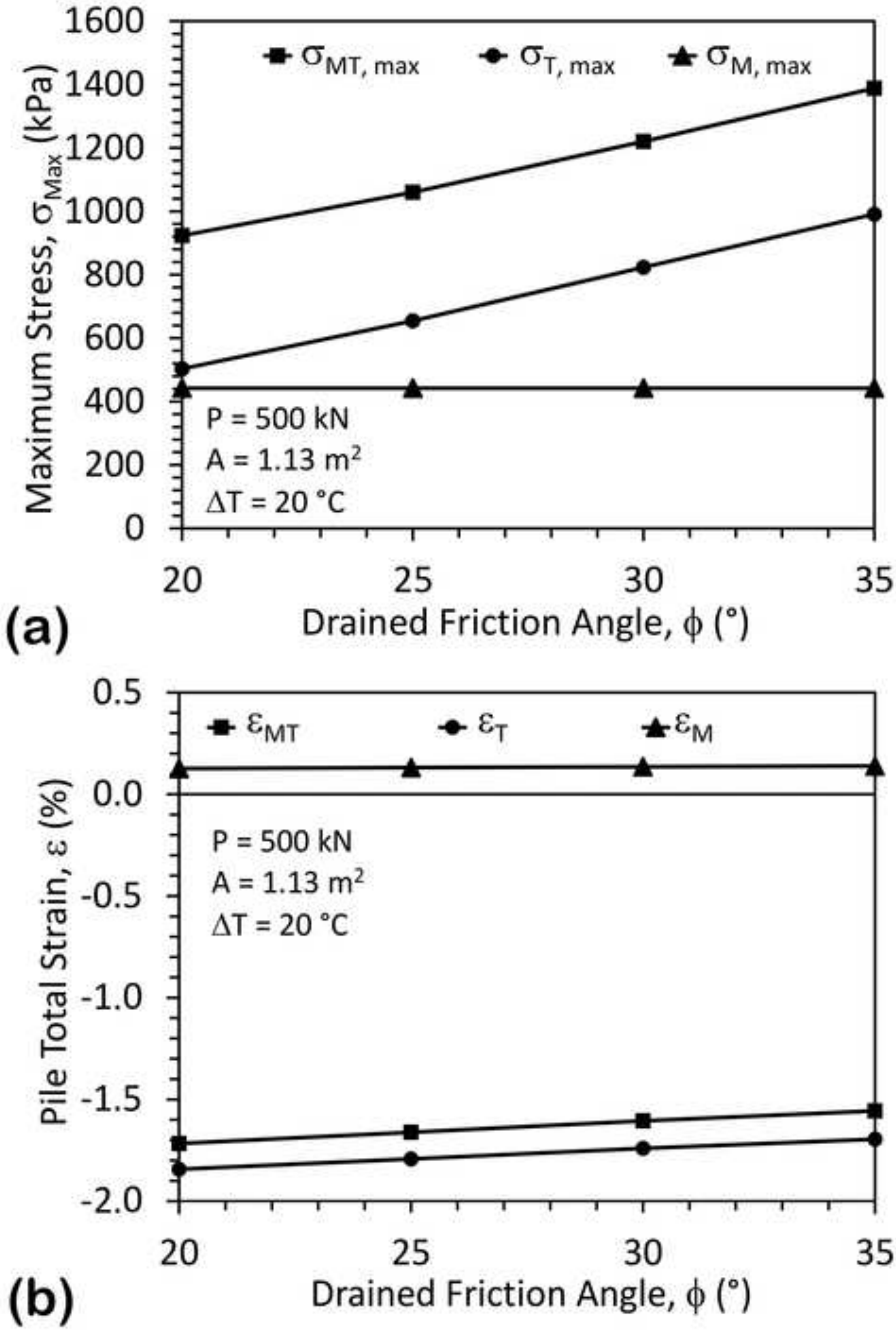

Figure 5

Click here to download Figure Figure 5.tif

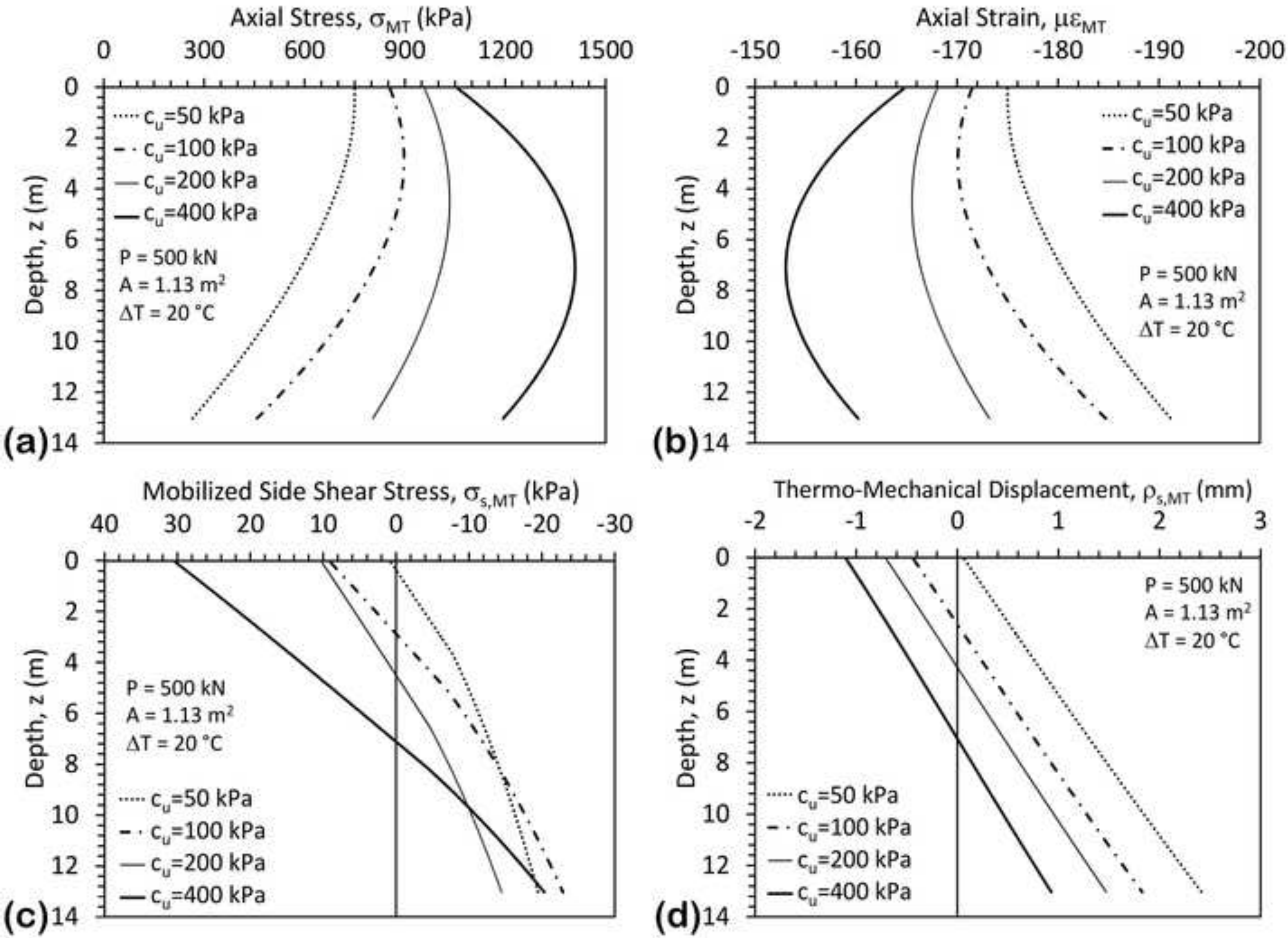

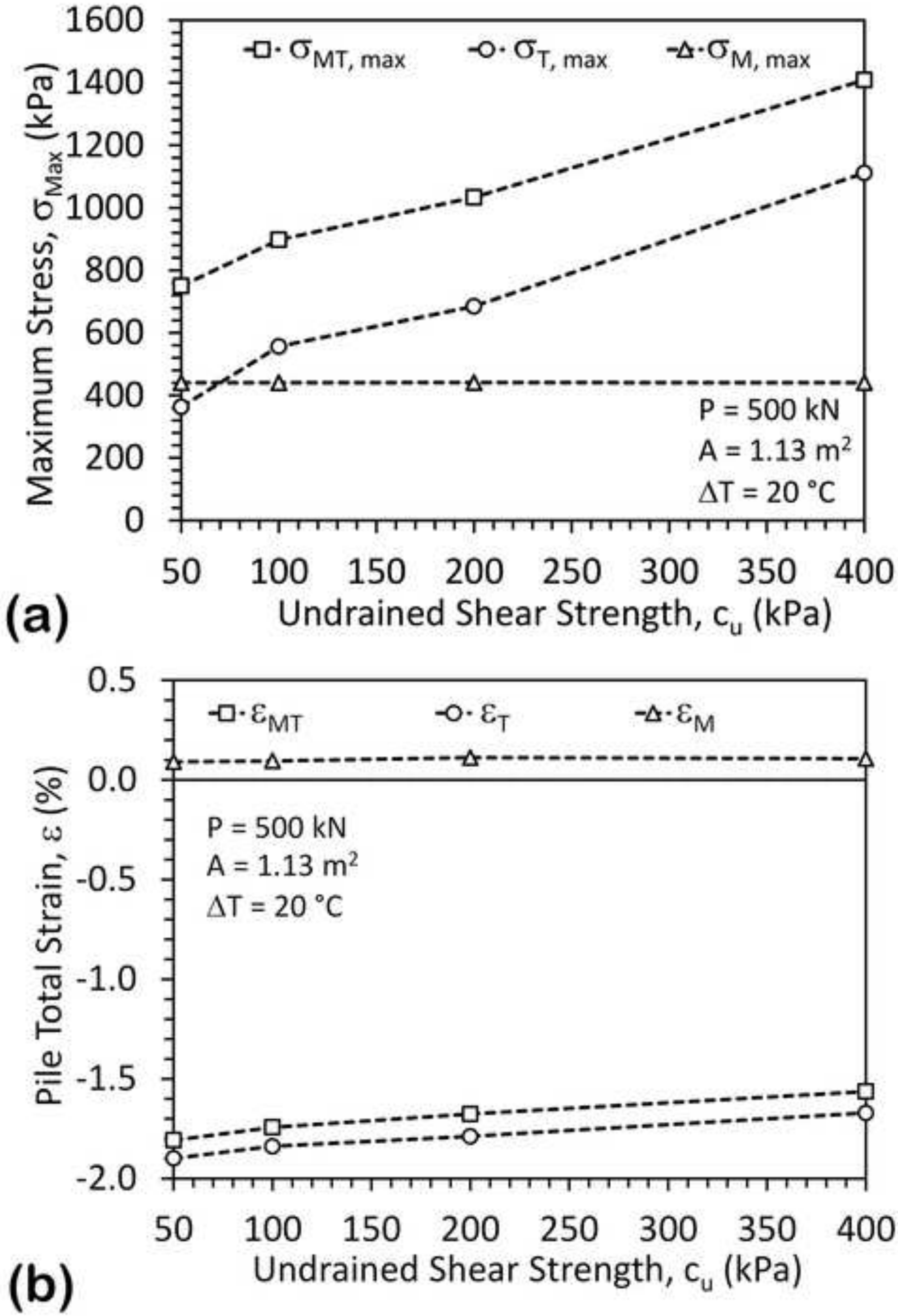
σMT, max
σT, max
σM, max
P = 500 kN
A = 1.13 m²
ΔT = 20 °C
Maximum Stress, σMax (kPa)
Undrained Shear Strength, cu (kPa)
(a)
εMT
εT
εM
P = 500 kN
A = 1.13 m²
ΔT = 20 °C
Pile Total Strain, ε (%)
Undrained Shear Strength, cu (kPa)
(b)

Figure 7

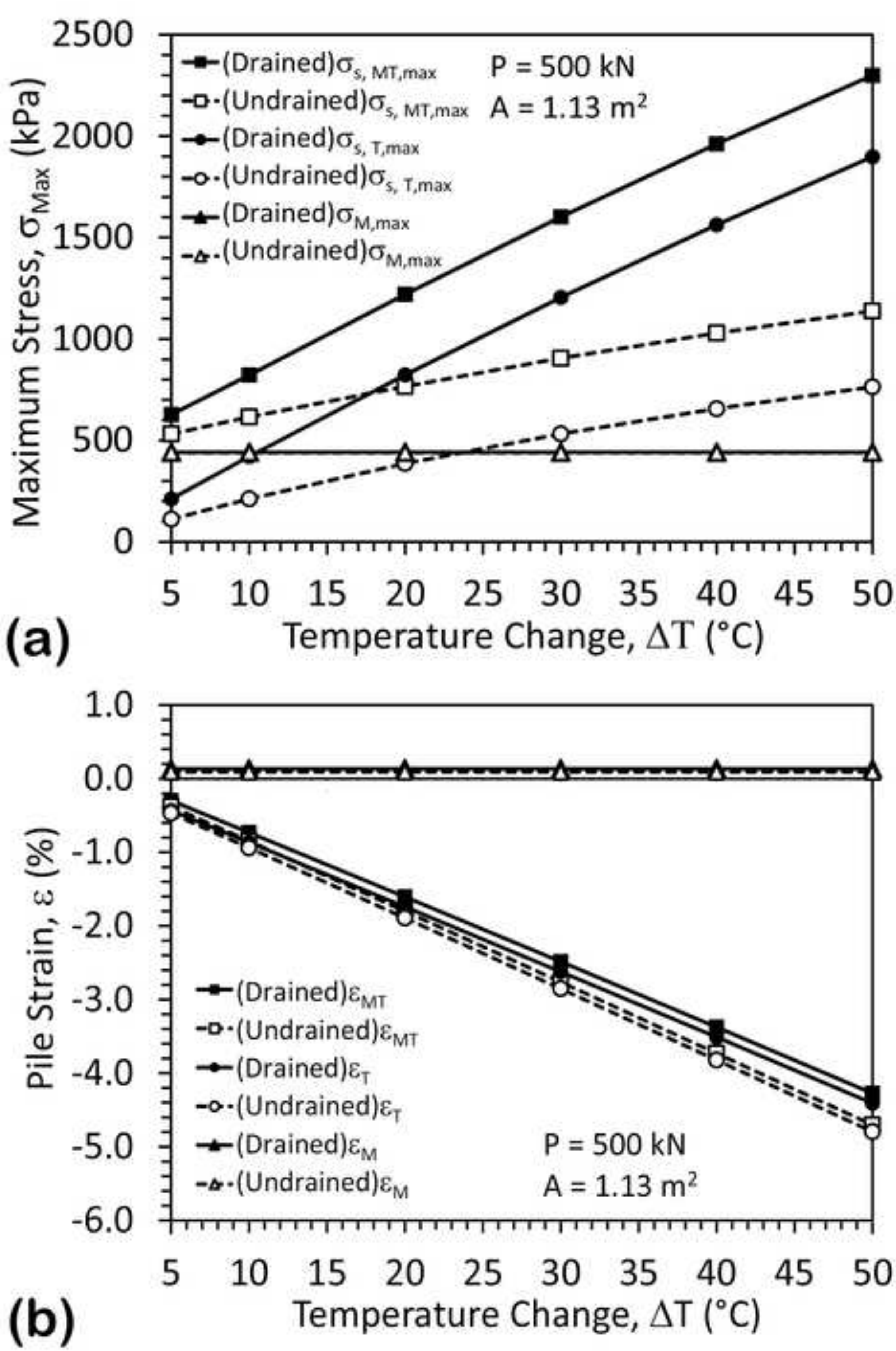

2500
2000
1500
1000
500
0
Maximum Stress, σMax (kPa)
(Drained)σs, MT,max
(Undrained)σs, MT,max
(Drained)σs, T,max
(Undrained)σs, T,max
(Drained)σM,max
(Undrained)σM,max
P = 500 kN
A = 1.13 m2
5 10 15 20 25 30 35 40 45 50
Temperature Change, ΔT (°C)
(a)
1.0
0.0
-1.0
-2.0
-3.0
-4.0
-5.0
-6.0
Pile Strain, ε (%)
(Drained)εMT
(Undrained)εMT
(Drained)εT
(Undrained)εT
(Drained)εM
(Undrained)εM
P = 500 kN
A = 1.13 m2
5 10 15 20 25 30 35 40 45 50
Temperature Change, ΔT (°C)
(b)

Figure 8

Click here to download Figure Figure 8.tif

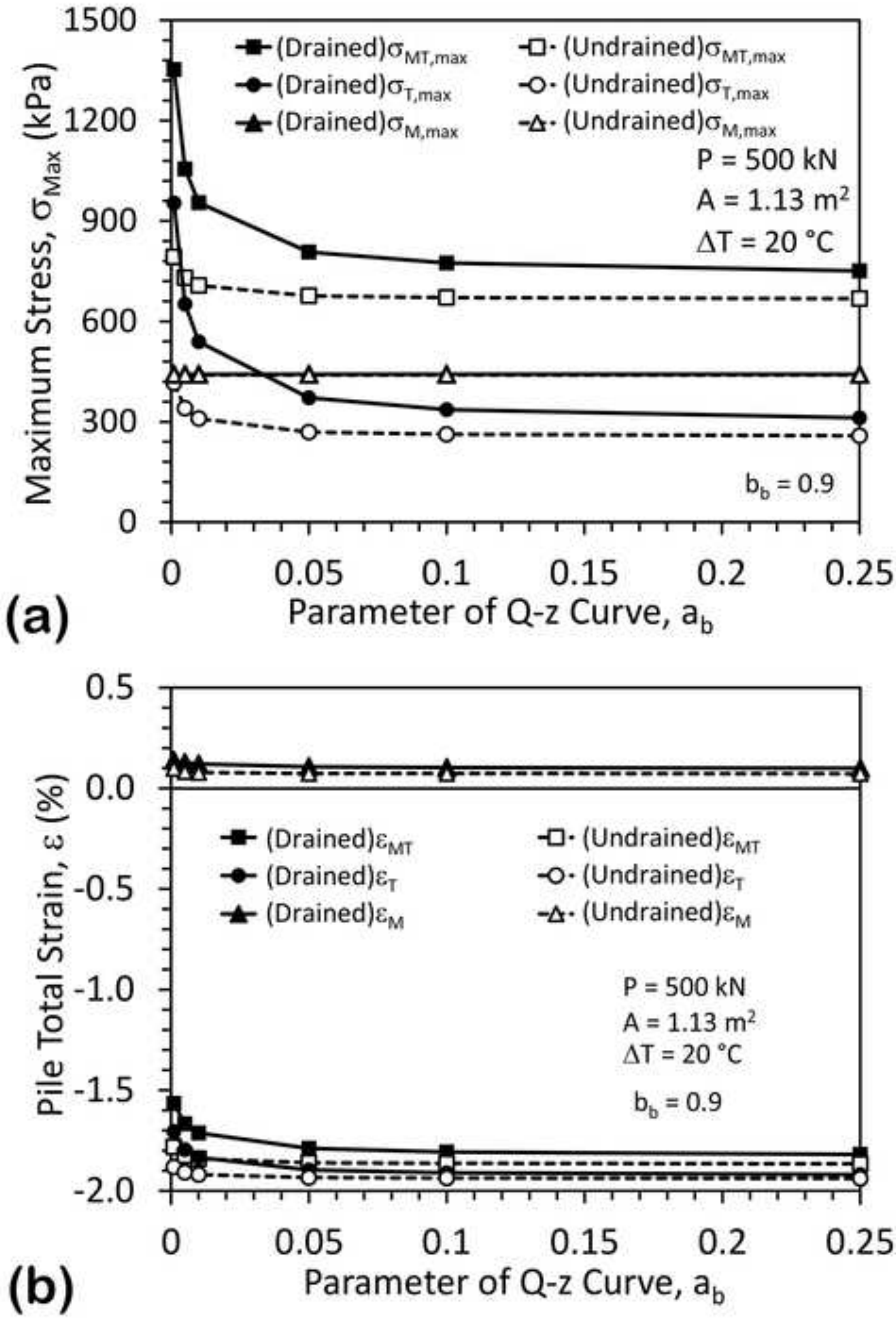

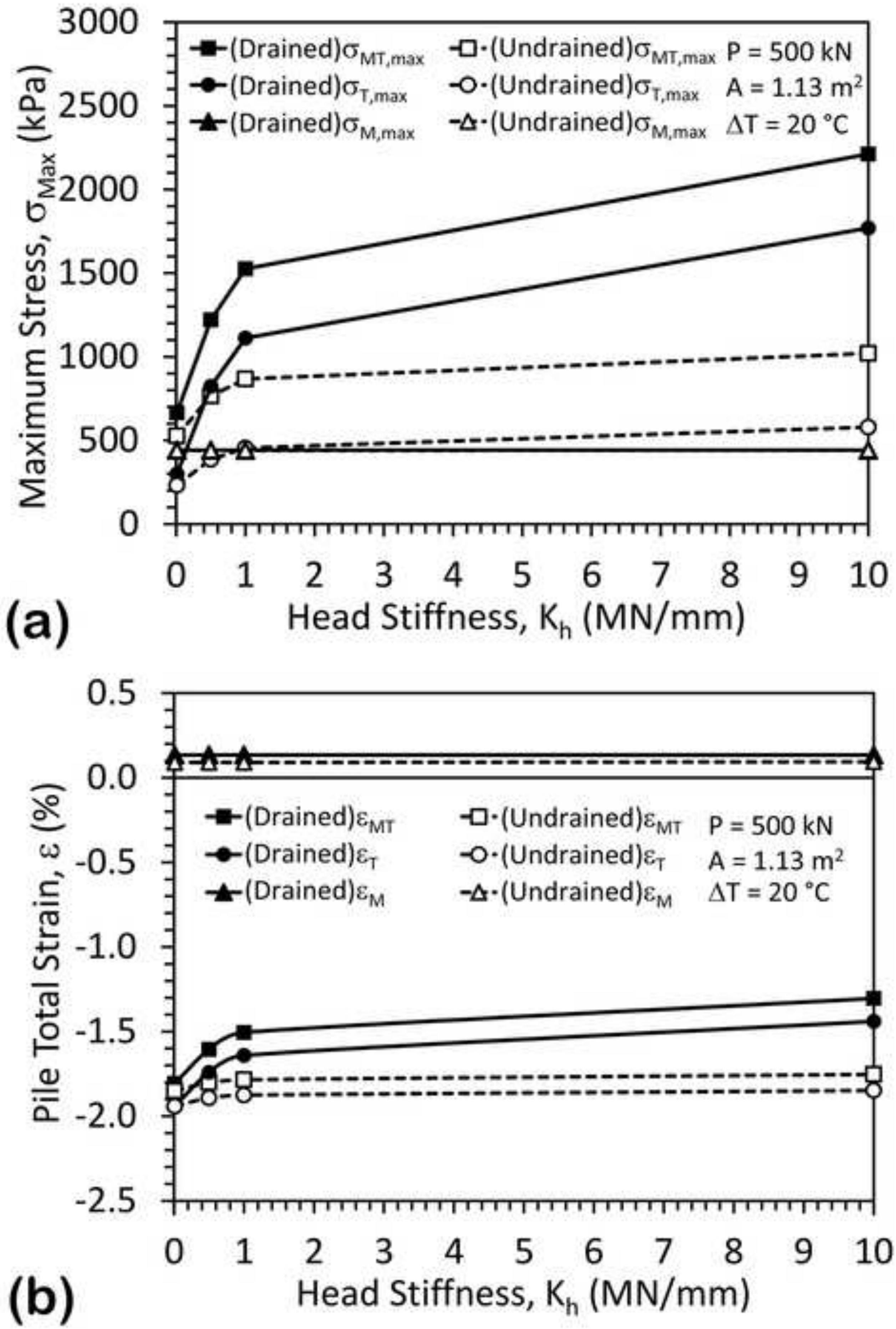

3000
2500
2000
1500
1000
500
0
Maximum Stress, σ_{Max} (kPa)
(Drained)$\sigma_{MT,max}$
(Drained)$\sigma_{T,max}$
(Drained)$\sigma_{M,max}$
(Undrained)$\sigma_{MT,max}$
(Undrained)$\sigma_{T,max}$
(Undrained)$\sigma_{M,max}$
P = 500 kN
A = 1.13 m^2
ΔT = 20 °C
0 1 2 3 4 5 6 7 8 9 10
Head Stiffness, K_h (MN/mm)
(a)
0.5
0.0
-0.5
-1.0
-1.5
-2.0
-2.5
Pile Total Strain, ε (%)
(Drained)ε_{MT}
(Drained)ε_T
(Drained)ε_M
(Undrained)ε_{MT}
(Undrained)ε_T
(Undrained)ε_M
P = 500 kN
A = 1.13 m^2
ΔT = 20 °C
0 1 2 3 4 5 6 7 8 9 10
Head Stiffness, K_h (MN/mm)
(b)

Figure 10

Click here to download Figure Figure 10.tif

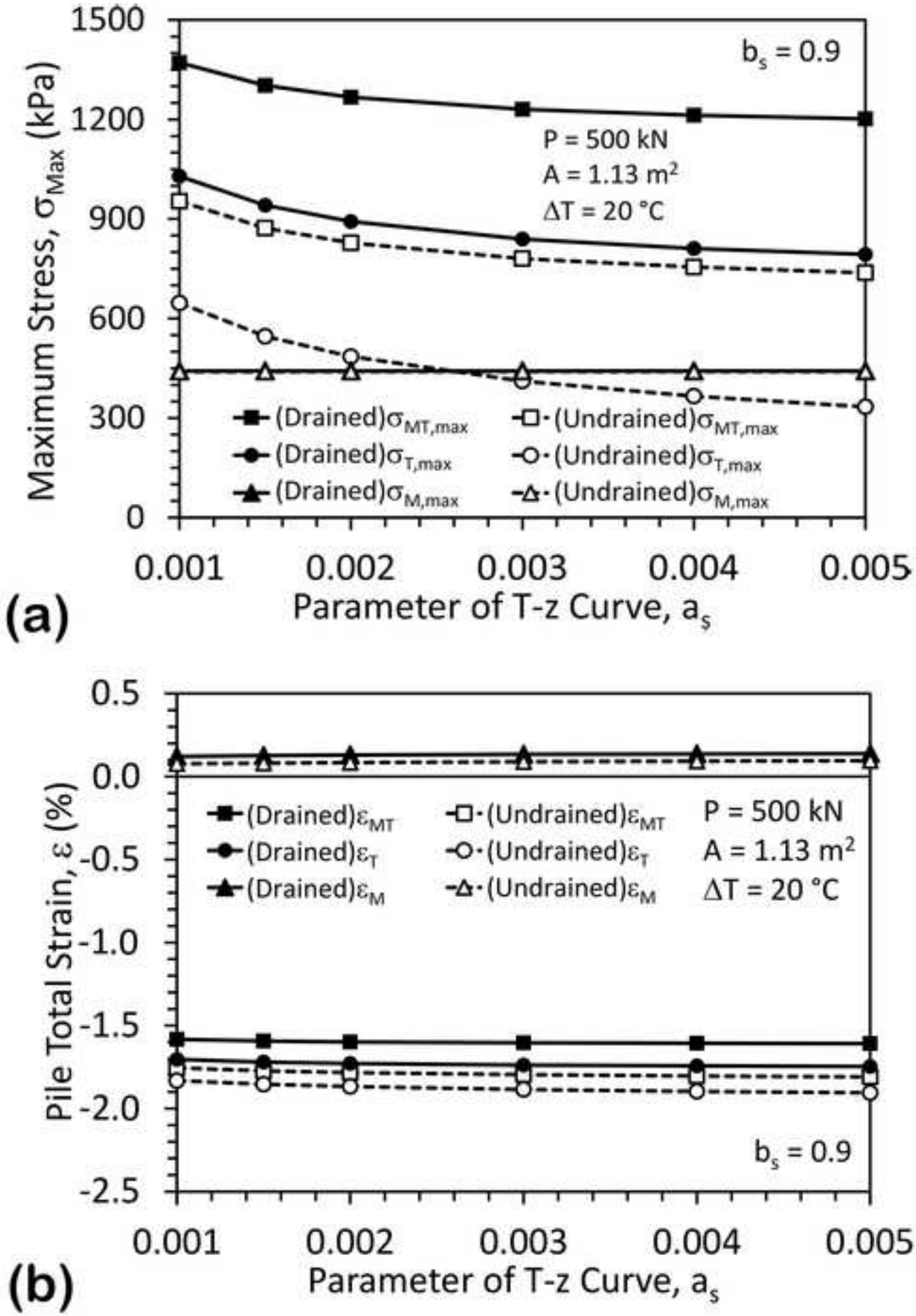

Figure 11 Click here to download Figure Figure 11.tif

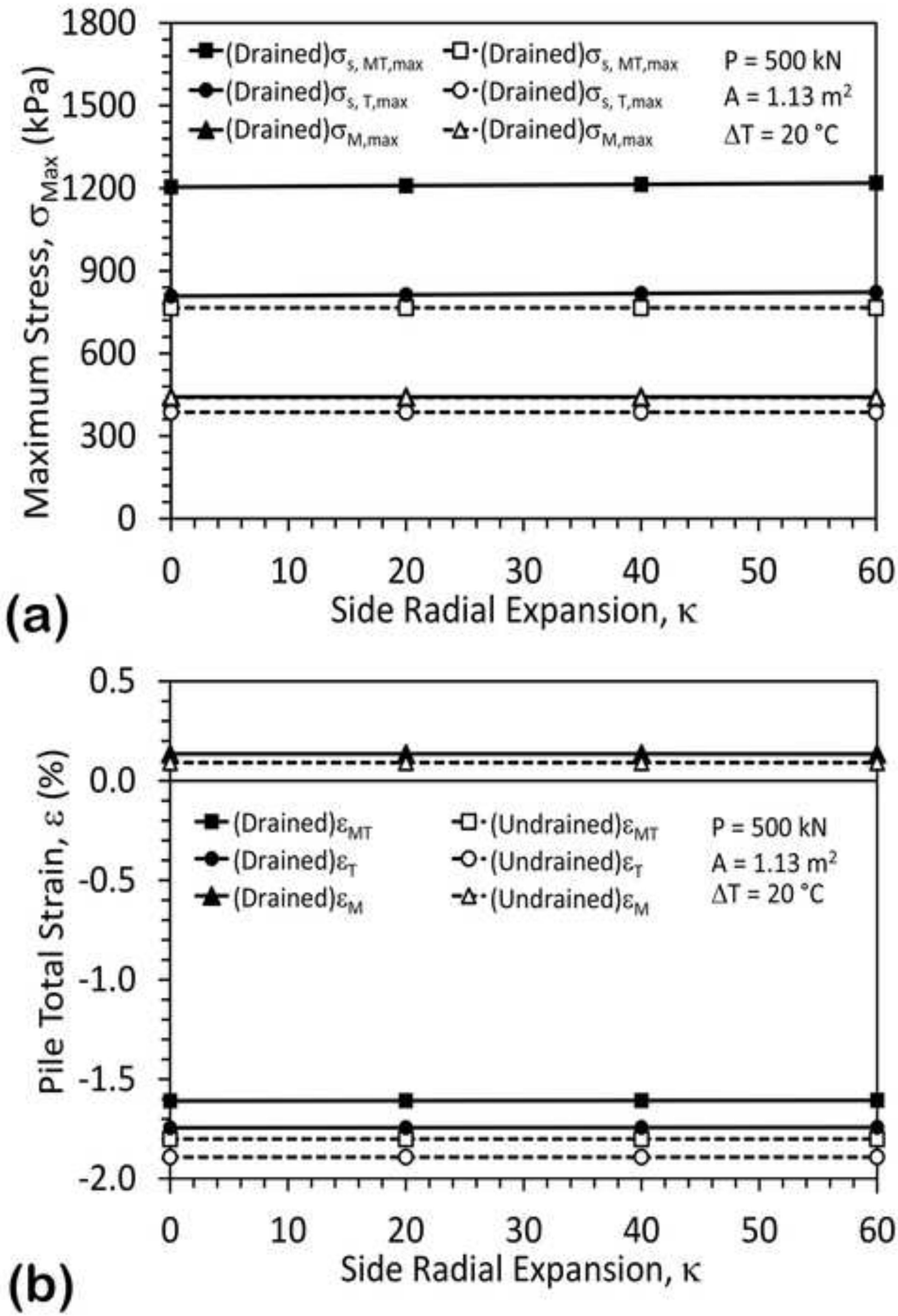

Figure 12

Click here to download Figure Figure 12.tif

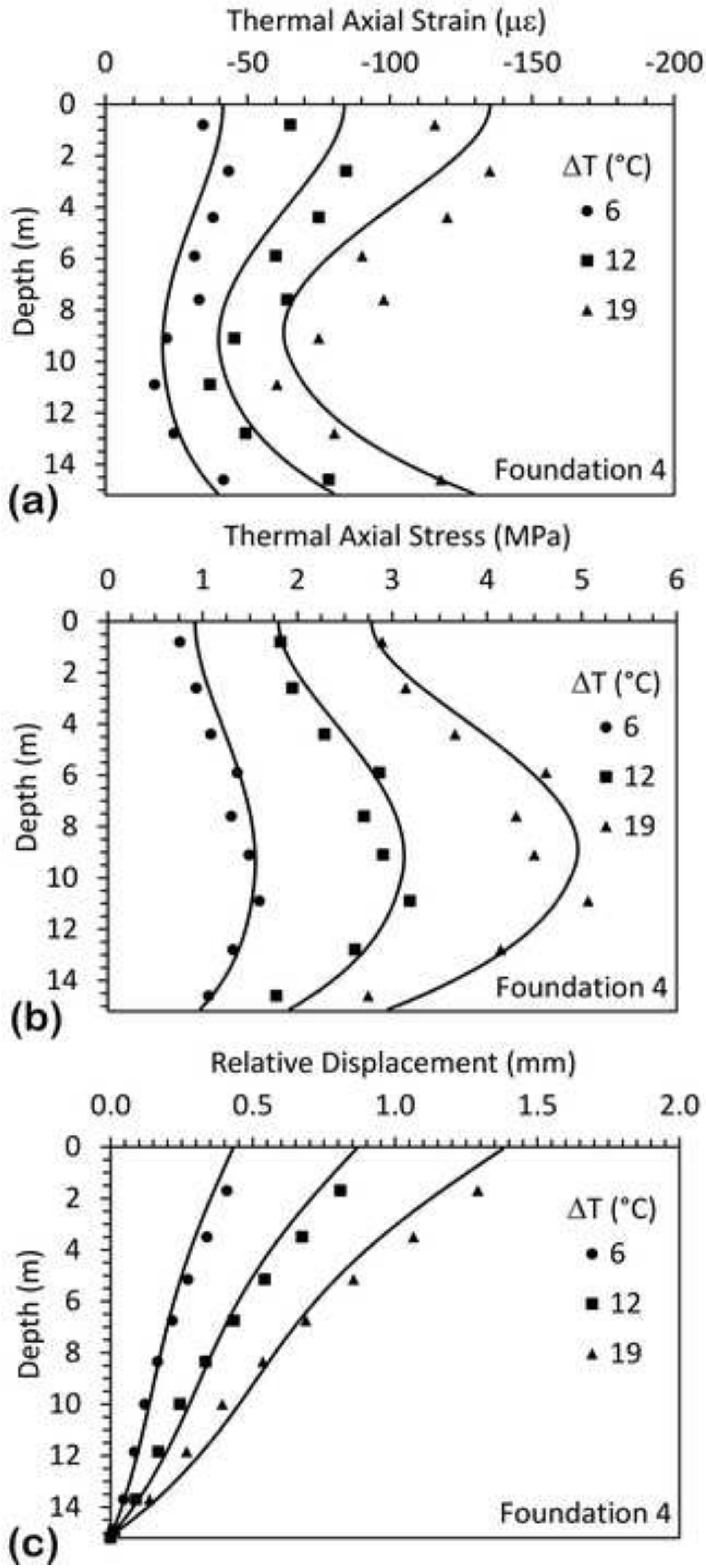

Figure 13

Click here to download Figure Figure 13.tif

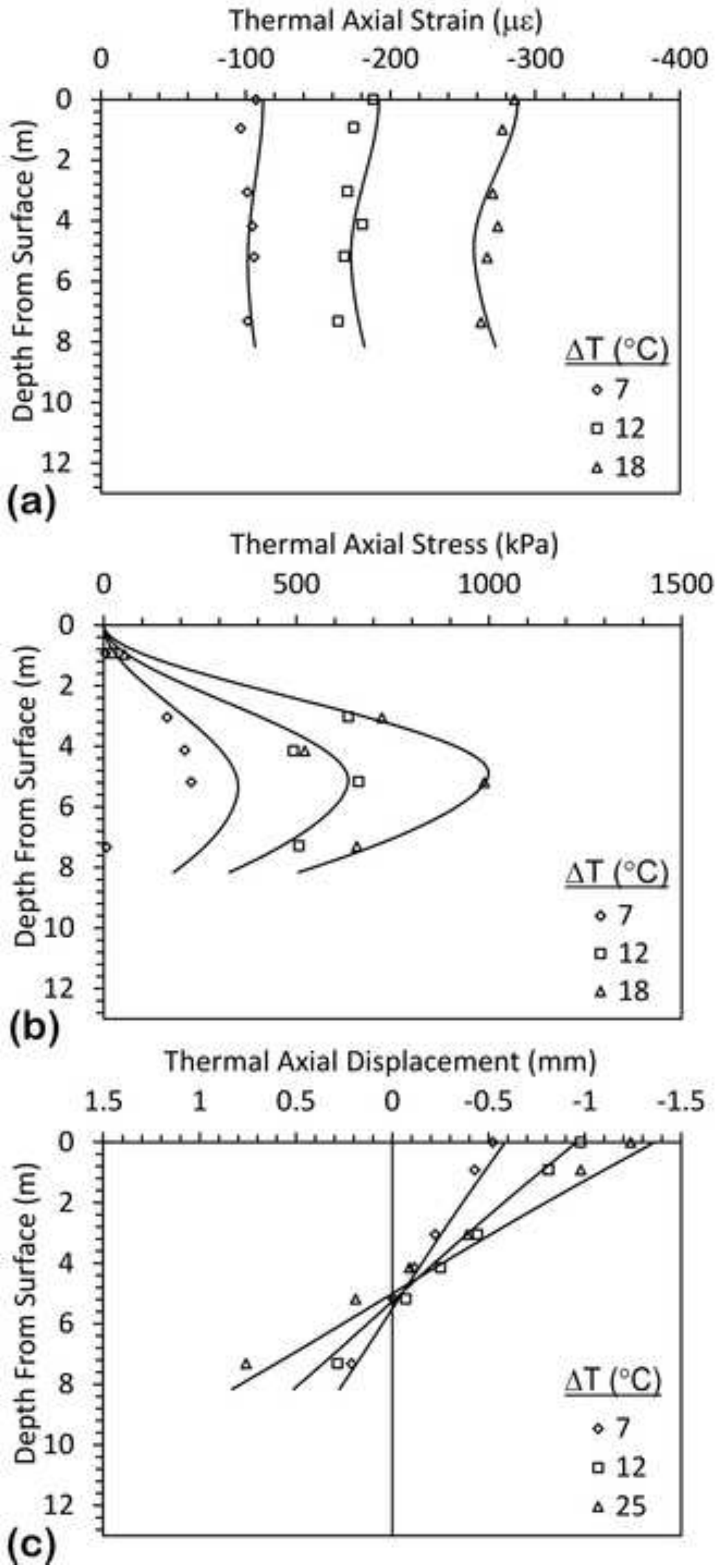

Figure 14

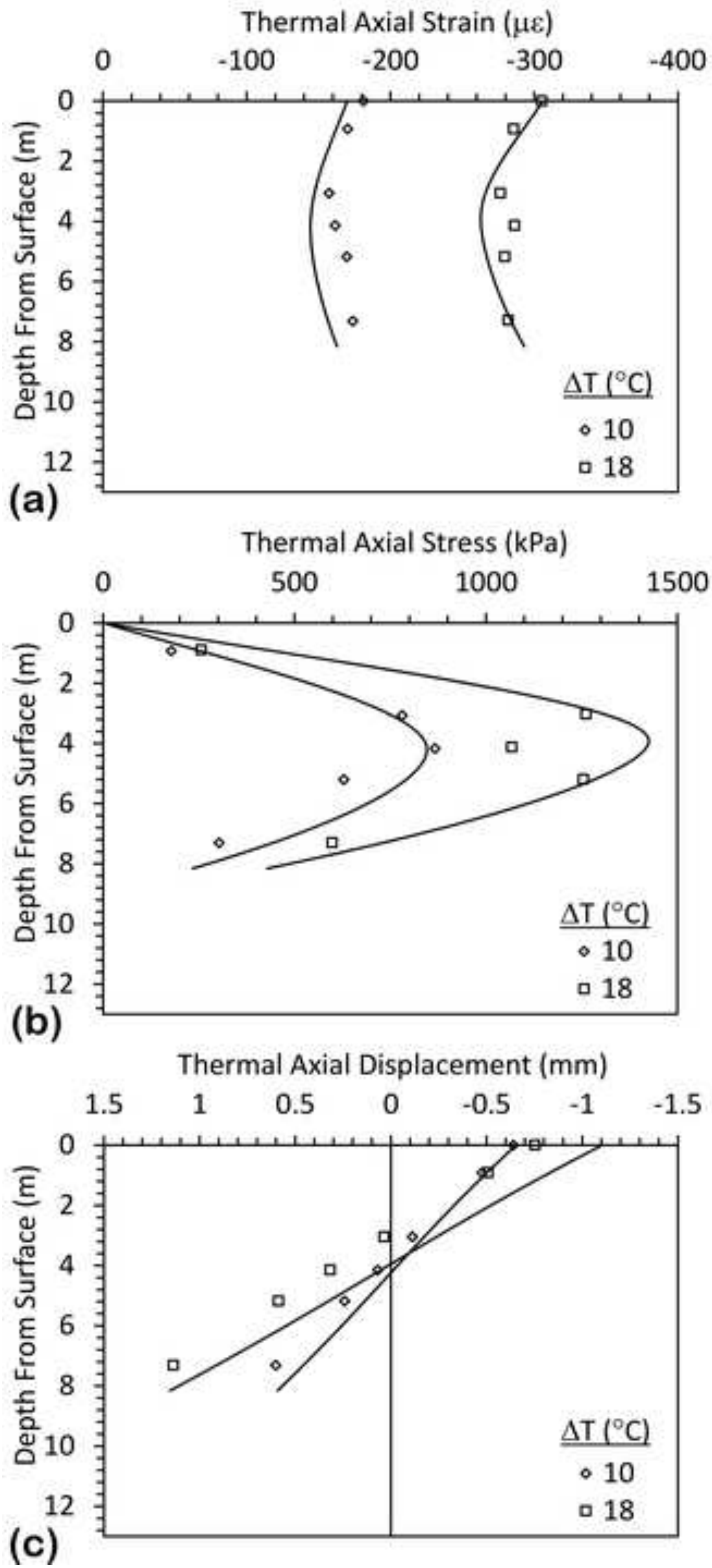
Thermal Axial Strain (με)
0
-100
-200
-300
-400
Depth From Surface (m)
0
2
4
6
8
10
12
ΔT (°C)
10
18
(a)
Thermal Axial Stress (kPa)
0
500
1000
1500
Depth From Surface (m)
0
2
4
6
8
10
12
ΔT (°C)
10
18
(b)
Thermal Axial Displacement (mm)
1.5
1
0.5
0
-0.5
-1
-1.5
Depth From Surface (m)
0
2
4
6
8
10
12
ΔT (°C)
10
18
(c)

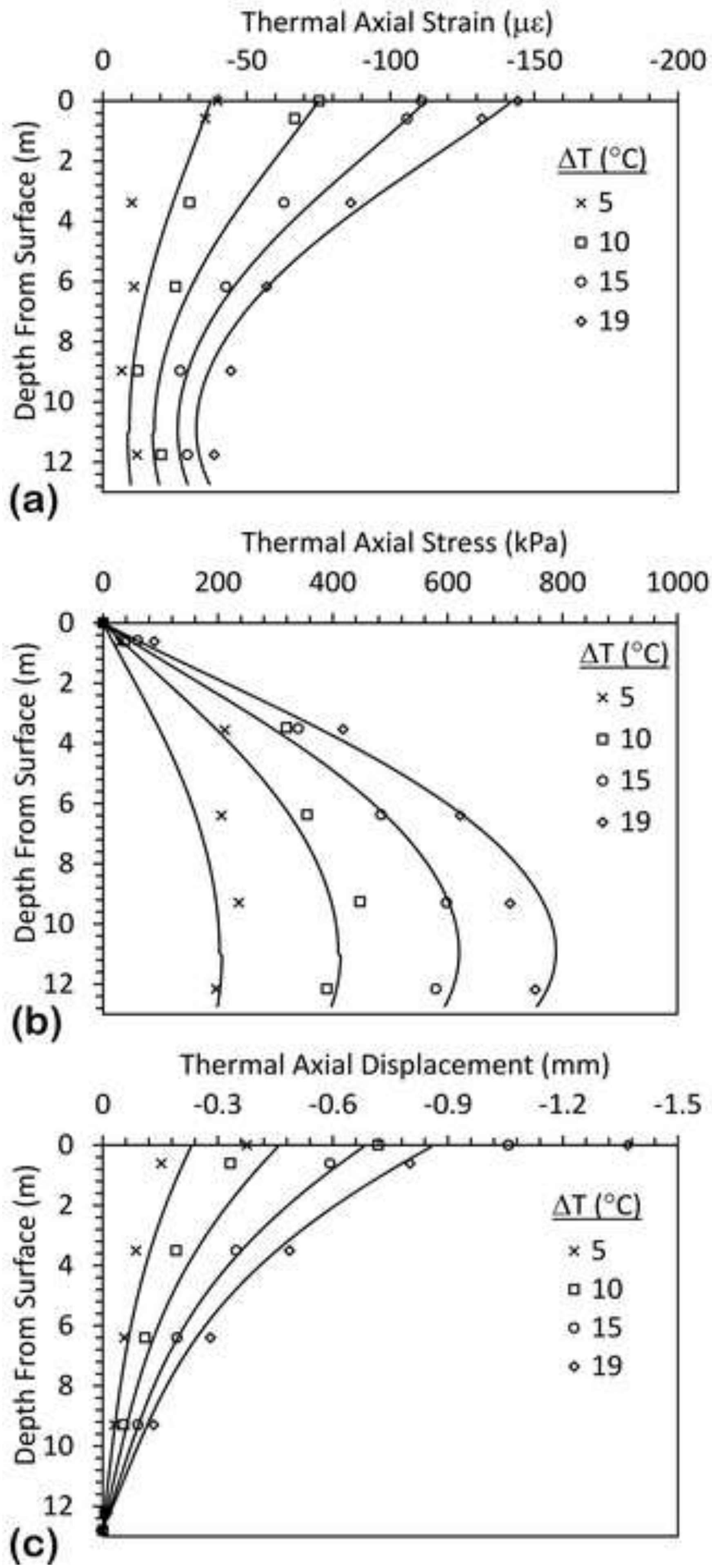

Thermal Axial Strain (με)
0
-50
-100
-150
-200
Depth From Surface (m)
ΔT (°C)
5
10
15
19
(a)
Thermal Axial Stress (kPa)
0
200
400
600
800
1000
Depth From Surface (m)
ΔT (°C)
5
10
15
19
(b)
Thermal Axial Displacement (mm)
0
-0.3
-0.6
-0.9
-1.2
-1.5
Depth From Surface (m)
ΔT (°C)
5
10
15
19
(c)

Figure 16

Click here to download Figure Figure 16.tif

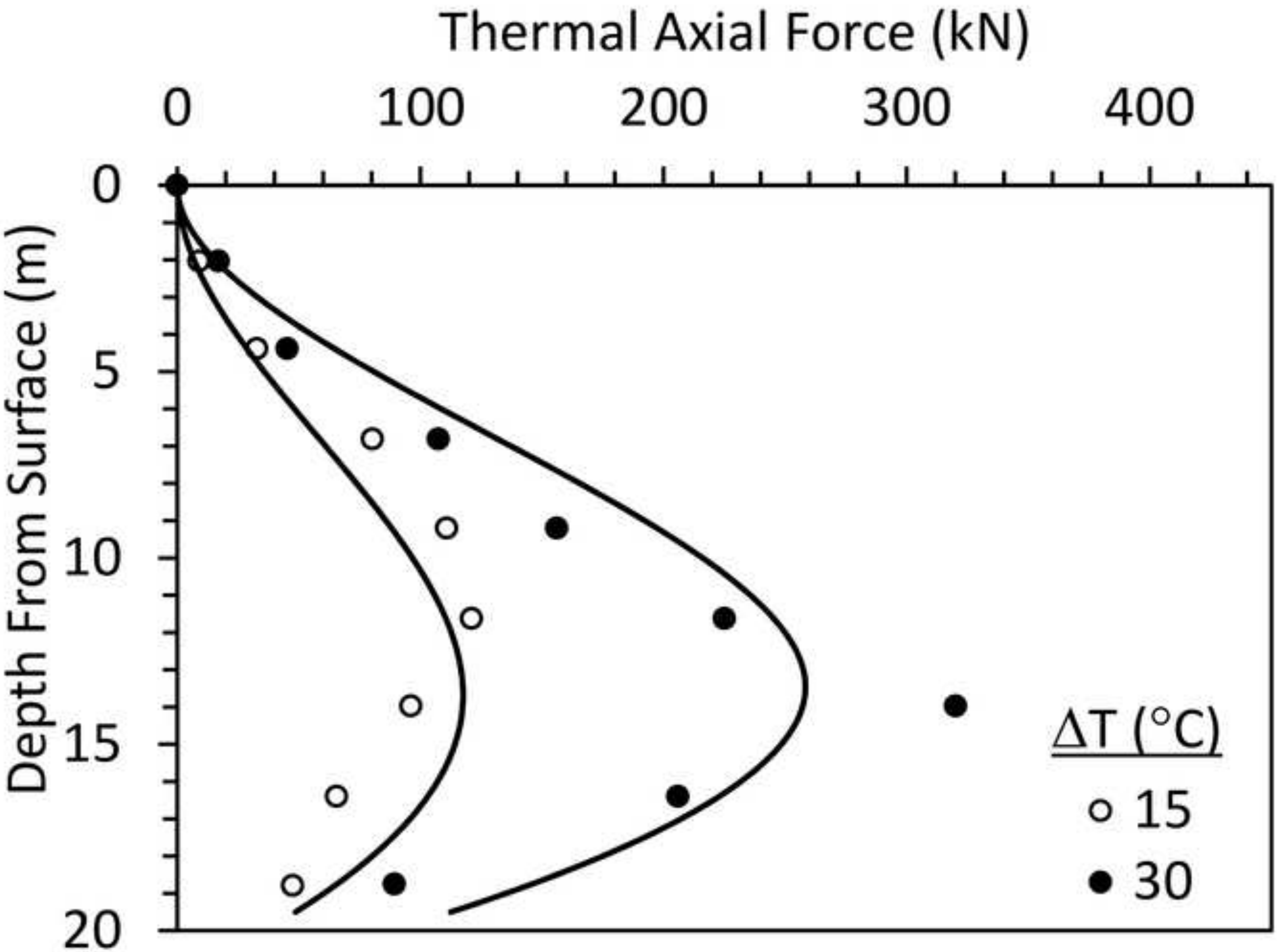

Figure 17

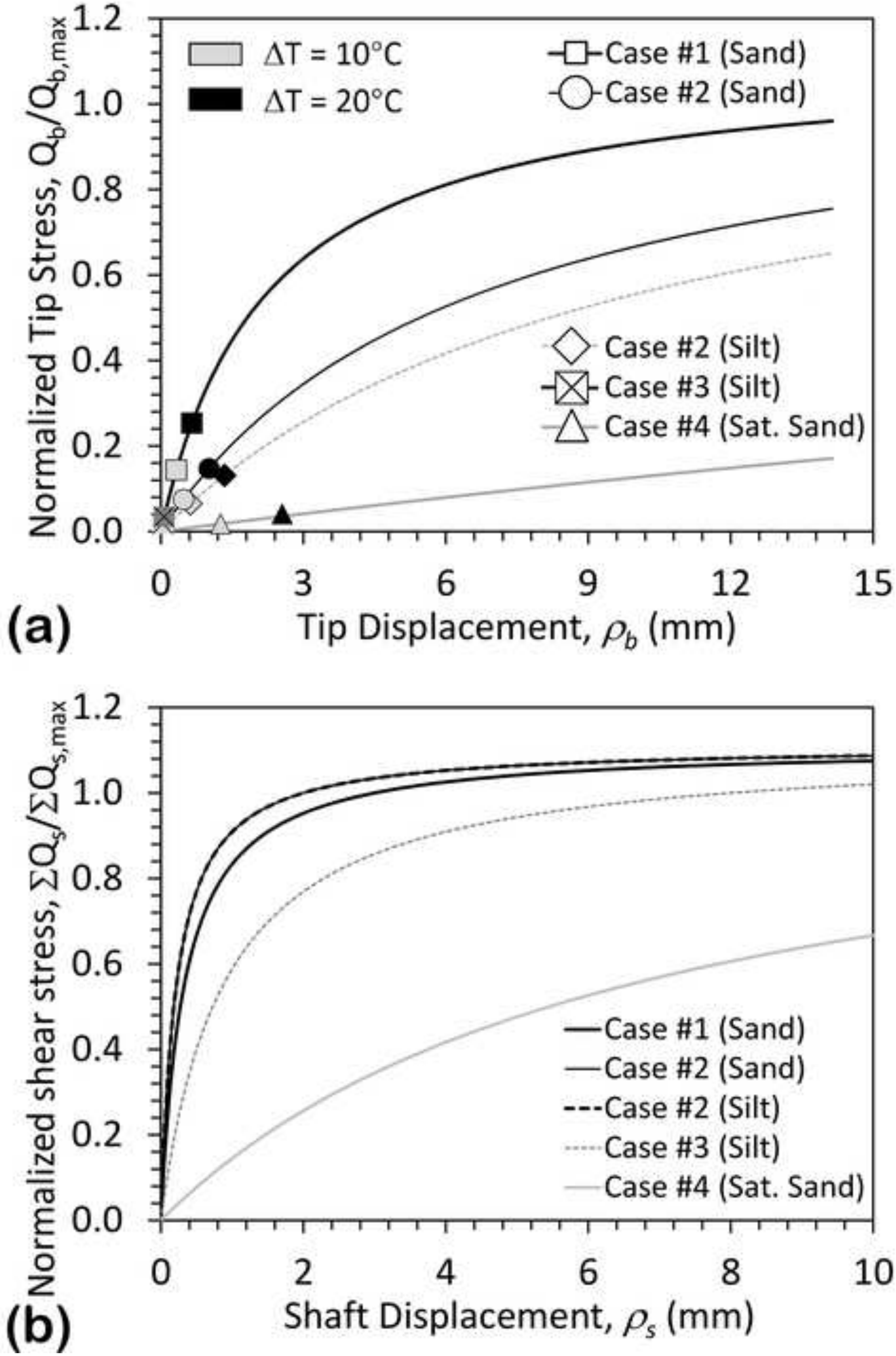

Normalized Tip Stress, $Q_b/Q_{b,max}$
1.2
1.0
0.8
0.6
0.4
0.2
0.0
ΔT = 10°C
ΔT = 20°C
Case #1 (Sand)
Case #2 (Sand)
Case #2 (Silt)
Case #3 (Silt)
Case #4 (Sat. Sand)
0
3
6
9
12
15
Tip Displacement, ρ_b (mm)
(a)
Normalized shear stress, $\Sigma Q_s/\Sigma Q_{s,max}$
1.2
1.0
0.8
0.6
0.4
0.2
0.0
Case #1 (Sand)
Case #2 (Sand)
Case #2 (Silt)
Case #3 (Silt)
Case #4 (Sat. Sand)
0
2
4
6
8
10
Shaft Displacement, ρ_s (mm)
(b)

Figure 18

Click here to download Figure Figure 18.tif

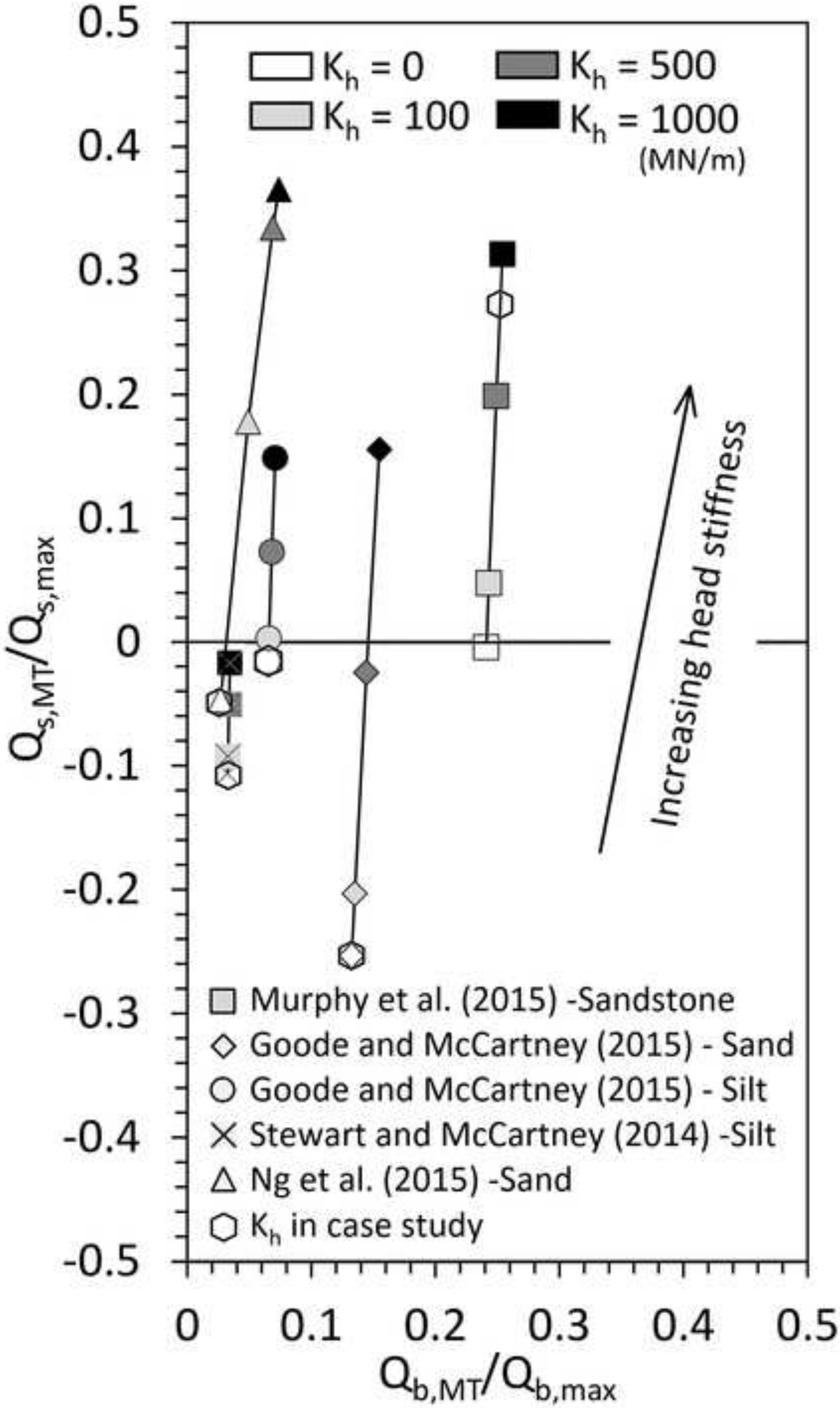

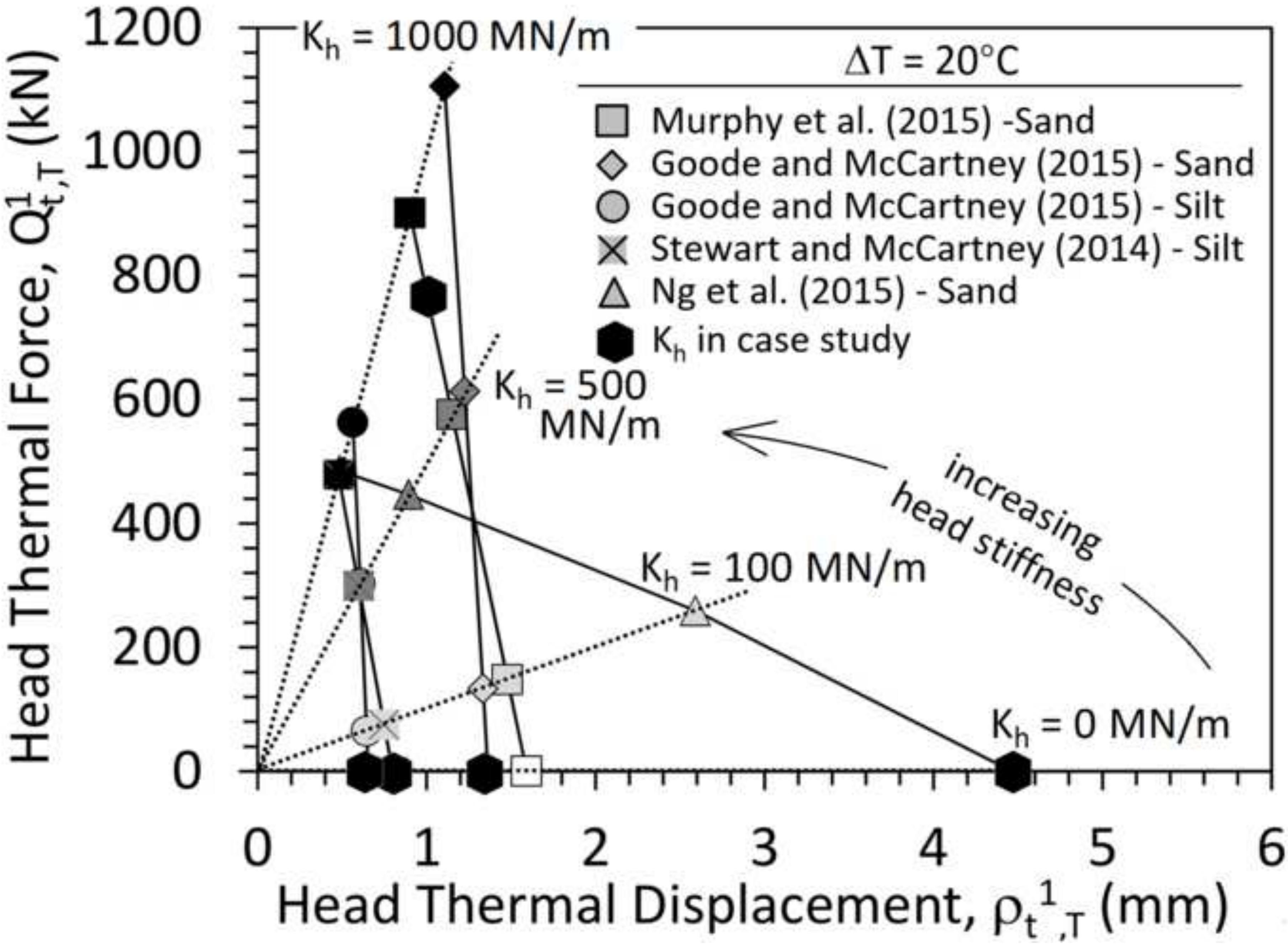

Head Thermal Force, $Q^1_{t,T}$ (kN)
1200
1000
800
600
400
200
0
0
1
2
3
4
5
6
Head Thermal Displacement, $\rho_t{}^1{}_{,T}$ (mm)
K_h = 1000 MN/m
ΔT = 20°C
Murphy et al. (2015) -Sand
Goode and McCartney (2015) - Sand
Goode and McCartney (2015) - Silt
Stewart and McCartney (2014) - Silt
Ng et al. (2015) - Sand
K_h in case study
K_h = 500 MN/m
increasing head stiffness
K_h = 100 MN/m
K_h = 0 MN/m